

University of  
**BRISTOL**

**School of Chemistry**

Large Area Hot Filament CVD

William J. Rivers

**This thesis is submitted in partial fulfilment of the requirements for the Honours  
Degree of BSc at the University of Bristol**

Paul May

Neil Fox

Bristol Diamond Group

## **Table of Contents**

1. Abstract.....	1
2. Acknowledgements.....	2
3. Introduction .....	3
3.1 Diamond.....	3
3.1.1 Structure .....	3
3.1.2 Properties and Applications.....	3
3.1.3 Formation.....	4
3.2 Chemical Vapour Deposition .....	5
3.2.1 Reactants.....	5
3.2.2 Activation .....	6
3.2.3 Gas Phase Reactions .....	6
3.2.4 Deposition .....	6
3.2.5 Newly Proposed Diamond Growth Mechanism.....	8
3.3 Reactor Types.....	9
3.3.1 Hot Filament CVD.....	9
3.3.2 Microwave Plasma CVD .....	11
3.3.3 Point-Arc Remote Plasma CVD.....	11
3.4 Large Area CVD .....	13
3.4.1 Upscaling HFCVD.....	13
3.4.2 Upscaling MPCVD.....	14
3.4.3 Substrate Upscaling .....	18
3.5 Project Context .....	21
4. Experimental Method .....	25
4.1 Experimental Aims .....	25
4.2 Samples .....	25
4.3 Seeding.....	26
4.4 Reactor Design .....	27
4.5.1 Filament Arrangement.....	28
4.5.2 Filament Heating.....	29
4.5.3 Filament Carburization.....	30
4.6 Reactor Operation.....	30
4.7 Shutting down.....	31
4.8 Experiments .....	31
5. Commissioning of the Large Area HF CVD Reactor.....	32
5.0 Raman Characterisation.....	32

5.1 Results.....	33
5.2 Discussion.....	35
5.2.1 Samples TS2-3 .....	35
5.2.2 Samples TS4-5 .....	36
6. Growth of ISIS Electron Stripping Films .....	39
6.1 Results.....	39
6.2 Discussion.....	41
6.2.1 IS1.....	41
6.2.2 IS2.....	42
6.2.3 IS3.....	43
6.2.4 IS4.....	44
7. Conclusions .....	46
7.1 Summary .....	46
7.2 Future work.....	47
8. References .....	48
9. Appendix 1: Sample IS5.....	51

## **1. Abstract**

Diamond has a vast array of extreme physical and chemical properties, however due to these properties it is extremely difficult to work with. Chemical vapour deposition (CVD) has allowed the properties diamond to be harnessed, for a wide variety of applications. CVD technology however has been limited by small areas of deposition for future real world applications.

The primary aim of this research was to commission the Bristol Diamond Groups large area HF CVD reactor. To commission the reactor diamond was deposited on seeded Si plates ( $30 \times 50$  mm) using  $4 \times 7$  cm Ta filaments at 466 W and gas composition of 1 % CH<sub>4</sub> in H<sub>2</sub>. The quality was then analysed by Raman spectroscopy. Raman spectra showed strong diamond peaks at  $1332 \text{ cm}^{-1}$  and low graphitisation across all deposited films. The results showed the reactor can able to deposit high quality polycrystalline diamond films over a given area ( $30 \times 50$  mm), provided the surface was within a 5 mm radius of a hot filament. The reactor has the capacity for  $15 \times 15$  cm wafers and with the installation of a larger power supply the work indicates high quality diamond films will be able to be deposited over areas of this size.

The secondary aim of this research was to grow diamond electron stripping foils for the ISIS neutron and muon source, to the required specifications for use in their accelerator facility. Five diamond foils (IS1-5) were grown on patterned Si plates ( $30 \times 55$  mm) using the large area HF CVD reactor. The samples were single or double seeded with nanodiamond and grown using  $4 \times 7$  cm Ta filaments at a power of 466 W and 1 - 1.5 % CH<sub>4</sub> in H<sub>2</sub>. The surfaces exhibited a uniform diamond layer across their smooth and patterned areas. Raman data showed the films exhibited strong diamond peaks at  $1332 \text{ cm}^{-1}$  and high film purities. It was found that double seeded samples grown for a longer time period (4 h) at 1 % CH<sub>4</sub> yielded the most crystalline samples with the fewest number of pin-holes under microscope. The aim was partially met as high quality diamond films were deposited over the required area and patterned surfaces, however, further work is required to quantitatively assess the thickness and number of pin-holes before the samples can be used in the ISIS accelerator facility.

## **2. Acknowledgements**

After reading his PhD many times during my project, I have decided to dedicate it to Paul Masons wife Sherri who reminds him that anything is possible. Anything apart from free time and fixing a methane leak through a valve.

Joking aside I would like to thank the members of the Bristol Diamond Group for their help during my project. In particular I would like to thank Professor Paul May and Dr James Smith for their guidance and help from start to finish, without whom this project really would not have been possible.

I would also like to thank Dr Jean-Charles Eloi of the University of Bristol's Chemical Imaging Facility for taking the SEM photographs.

I would like to thank my friends and flat mates for their help and support throughout this year.

Finally I would like to thank my family for their unwavering support throughout this project and throughout the course of my degree. They gave me the opportunity to pursue a degree in a subject I am passionate about and I hope to make them proud. Truly I cannot thank them enough.

*I came into this project thinking pressure makes diamonds, I left knowing that 20 Torr and a few thousand degrees also does the trick.*

### **3. Introduction**

Diamonds hold vast cultural importance, as precious stones, in engagement rings and co-starring with Sean Connery in 1971's 'Diamonds are Forever'. Aside from being 'a girl's best friend', the vast array of extreme physical and chemical properties of diamond, if harnessed, could also make them a valuable engineering material. This review focuses on the growth of diamond by chemical vapour deposition (CVD) and the challenges faced in large area growth.

#### **3.1 Diamond**

##### **3.1.1 Structure**

Diamond has a tetrahedral lattice structure of  $sp^3$  hybridised carbon atoms (fig. 1). Diamond exists in several forms: single crystal as in gemstones, single crystalline plates as grown in CVD, powders as used for coatings and as polycrystalline plates which are also grown synthetically but consist of multiple crystals<sup>1</sup>. Natural diamonds mainly exist in octahedral cubic crystals with (111) planes<sup>2</sup> whereas synthetic diamond mainly exist in simple cubic with (100) planes<sup>2</sup>.

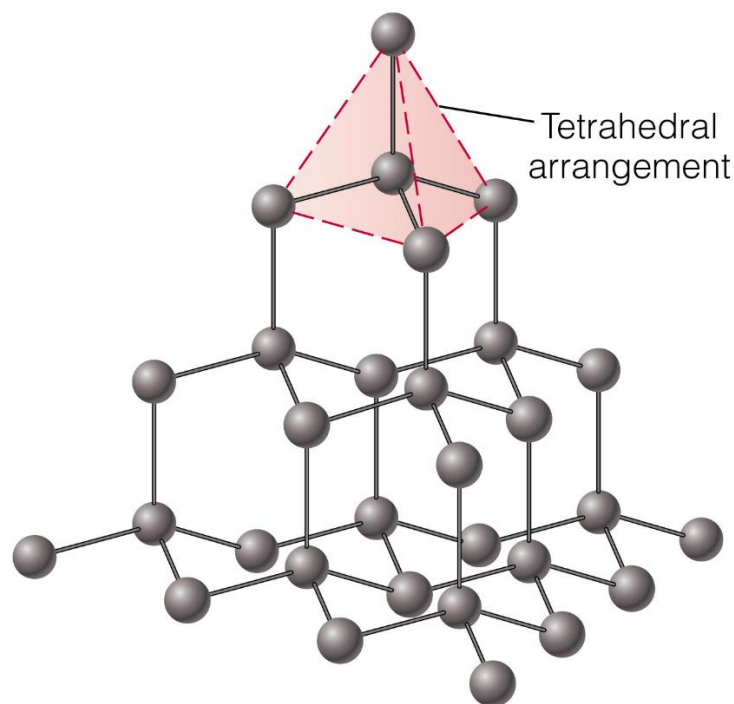


**Figure 1:** Ball and stick tetrahedral diamond lattice<sup>3</sup>

##### **3.1.2 Properties and Applications**

Diamond's extreme properties (Table 1) make it suited for a multitude of applications. Chemical inertness and extreme mechanical strength are optimal for biomedical applications. Nano-crystalline diamond (NCD) coated implants have been used on patients who have previously rejected uncoated implants<sup>4</sup>. Biocompatibility can be extended with conductive doped diamond. Boron doped diamond (BDD) has been shown to transmit electrical impulses between cells<sup>5</sup>. The electrode surface required daily acid regeneration for repeated use, a problem that would need to be solved before its use *in vivo*. Diamond and BDD may also have applications in brain computer interfaces having shown to be biocompatible with stem cell derived human neurons<sup>6</sup>. Further research is required as the laminin layer, which helps bind the neurons to the diamond, had to be replenished *in vitro*. *In vivo* this may pose an obstacle for permanent implants. One study found biocompatibility of long term (2-6 months) BDD implants *in vivo*, however the neuron-diamond connection was not monitored<sup>7</sup>. Further possible medical uses include BDD coated nano-needles which exhibit antibacterial properties by puncturing bacteria<sup>8</sup>.

Table 1: *Properties of Diamond at RTP*<sup>2</sup>

---

Chemical Inertness
Hardness (80 – 100 GPa)
Thermal Conductivity (up to 20 W cm <sup>-1</sup> K <sup>-1</sup> )
Young's Modulus (1050 GPa)
Debye Temperature (Around 2000K)
Linear Thermal Expansion Coefficient ( $1.2 \times 10^{-6}$ K <sup>-1</sup> )
Optical Transparency (At wavelengths above 225 nm)
Band Gap Width (5.4 eV)
Density (3.515 g cm <sup>-3</sup> )
Excitation Binding Energy (80 meV)

---

Diamonds extreme hardness means it is used in cutting tool coatings, extending tool lifetimes by up to  $\times 10$  compared with non-coated tools<sup>9</sup>. The thermal conductivity and low expansion co-efficient of diamond make it suited for use as a heat sink in electronic devices<sup>10, 11</sup>. Diamond foils have been shown to be highly efficient electron strippers in high powered (800 MeV) H<sup>-</sup> ion beams<sup>12</sup> (further discussed in section 3.5).

### **3.1.3 Formation**

Before the 1950's diamond was only naturally occurring, forming at high temperatures and pressures within the Earth's crust at some 140-200 km deep<sup>13</sup>. It only forms in such extreme conditions "because diamond is metastable, that is, kinetically stable but not thermodynamically stable"<sup>14</sup> and at RTP it is disfavoured over graphite. However, at RTP diamonds lattice stability prevents spontaneous conversion to graphite<sup>2</sup>. The first artificial diamonds were synthesised at ASEA in 1953, but the first commercial artificial diamonds were created by GE in 1954. GE's technique used multiple support bands on a high pressure cylinder allowing for pressure of up to 100,00 kg cm<sup>-3</sup> and temperature in excess of 2,300 °K to be achieved and diamond growth<sup>15</sup>. The use of chemical vapour deposition (CVD) for diamond growth was established in the 1980's by researchers at National Institute for Research in Inorganic Materials (NIRIM) in Japan. Since then CVD has blossomed to be a principle technique for artificial diamond growth.

### **3.2 Chemical Vapour Deposition**

The CVD process involves a gas phase reaction, creating reactive species which are then deposited on a substrate surface. The substrate may be of the same element (homoepitaxial) or a different element (heteroepitaxial) to that of the substrate. CVD systems have four major components (figure 2); (1) reactants, (2) activation, (3) gas phase reactions, (4) deposition.

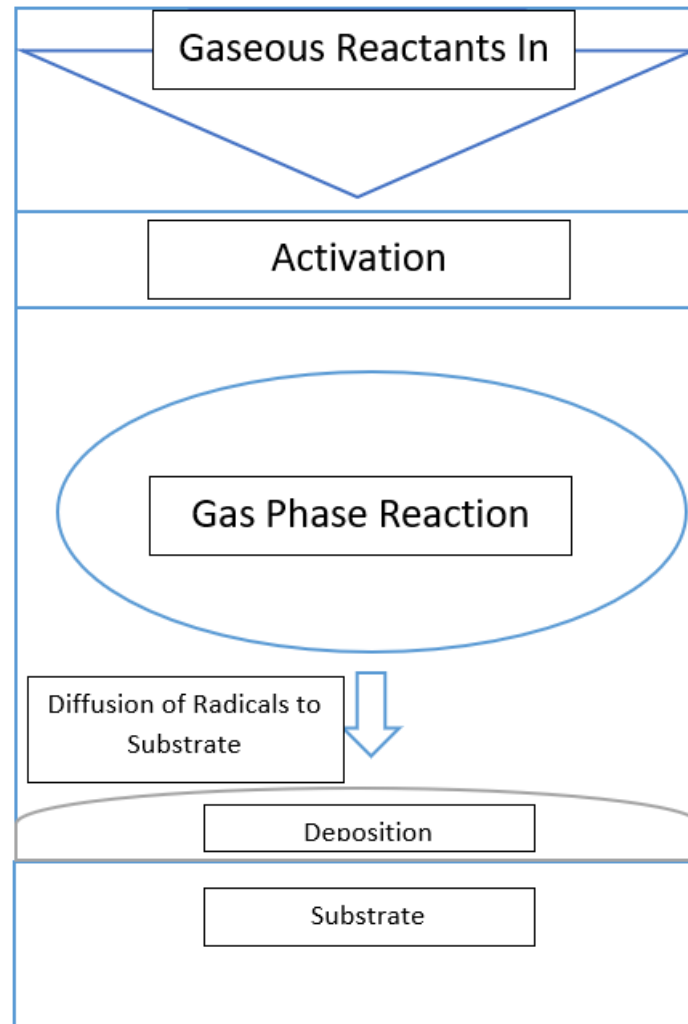


**Figure 2:** Major components of a CVD reactor system

#### **3.2.1 Reactants**

Diamond growth requires a short-chain carbon-containing reagent (usually methane, other hydrocarbons are available) as a carbon feedstock. Depending on the system and activation the concentration of  $\text{CH}_4$  can vary from 1~8 % vol<sup>14</sup> with the remainder of the gas mixture predominantly made up of hydrogen. The atomic H formed after activation terminates the surface bonds of the diamond lattice. Its main function however is the initiation of the series of gas phase chain reactions discussed in the next section. It also preferentially etches graphite, increasing diamond production<sup>16</sup>.

#### **Being inclusive with Argon (Ar)**

Ar is non-essential for CVD however, its addition with reactant gases has been shown to increase the growth rate during MPCVD<sup>17</sup>. It has also been shown to give an improved uniformity in temperature across the sample from a variance of 40% to > 10%, which promotes uniform growth and reduces lattice strain. Ar is also too bulky to diffuse throughout the diamond lattice, as with other additive

such as N, maintaining purity. For upscaling, reducing the amount of hydrogen gas is also more economically efficient as hydrogen generators must be continuously run to satisfy demand<sup>18</sup>.

### 3.2.2 Activation

The most important part of CVD is the activation of hydrogen to form radical species. The input energy used differentiates each CVD technique, as a unique reactor is required for each form. Most commonly reactors are either hot filament (HFCVD) or microwave plasma (MPCVD). However, many other sources can be used such as; direct current, radiofrequency, chemical, etc<sup>19</sup>... Reactor types are split into two groups heated gas (thermal or chemical) or a plasma (electrical or electromagnetic) technique<sup>20</sup>. It is not important which form of input energy is used so long as there is activation.

### 3.2.3 Gas Phase Reactions

The hydrogen chemistry underpins the rest of a CVD system's vapour and deposition chemistry. A schematic diagram of the different chemical reactions is shown in figure 3.

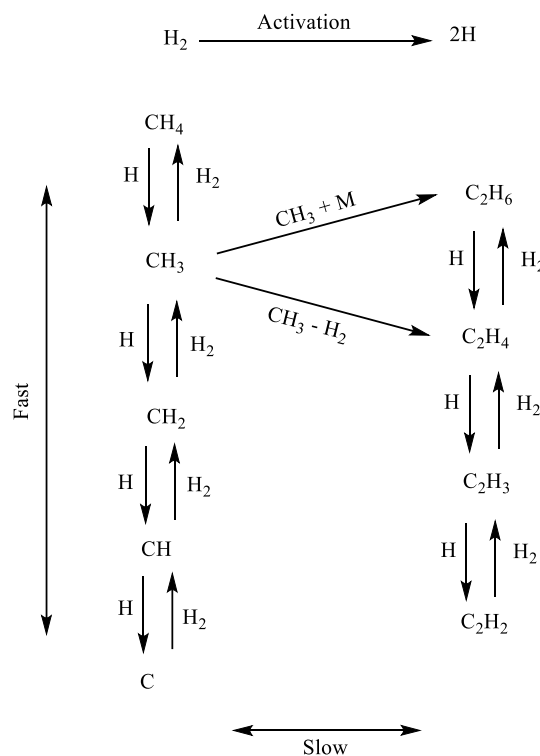


**Figure 3:** The major gas-phase reactions in a CVD system. Figure reproduced from [21].

The input energy first splits molecular hydrogen to atomic hydrogen (forming about 40% of the reaction mixture<sup>21</sup>). The low pressure creates a super equilibrium of atomic H, due to the slow recombination in the gas phase<sup>22</sup>. The atomic H then reacts with the carbon feed gas (usually methane) creating a range of carbon radicals. The gaseous intermediates spread out via diffusion and can then adsorb onto the solid substrate surface where they may react<sup>21</sup>.

### 3.2.4 Deposition

The concentration of atomic H drops near the surface due to recombination with surface terminating  $\text{sp}^3$  hydrogens<sup>21</sup>. This creates an active surface site with which radicals can react (figure 4). The carbon containing radicals then react with the active site forming a C-C bond. The adsorbed carbons can themselves become active sites and react with adjacent carbons. Through the adsorption of carbon radicals across the substrate, the lattice begins to build up. However this can be in the form of both  $\text{sp}^3$  diamond and  $\text{sp}^2$  graphite. As mentioned before, however, graphite is etched away by atomic H at a

much higher rate than diamond<sup>16</sup>. Hence, CVD growth is diamond and graphite production followed by graphite removal.

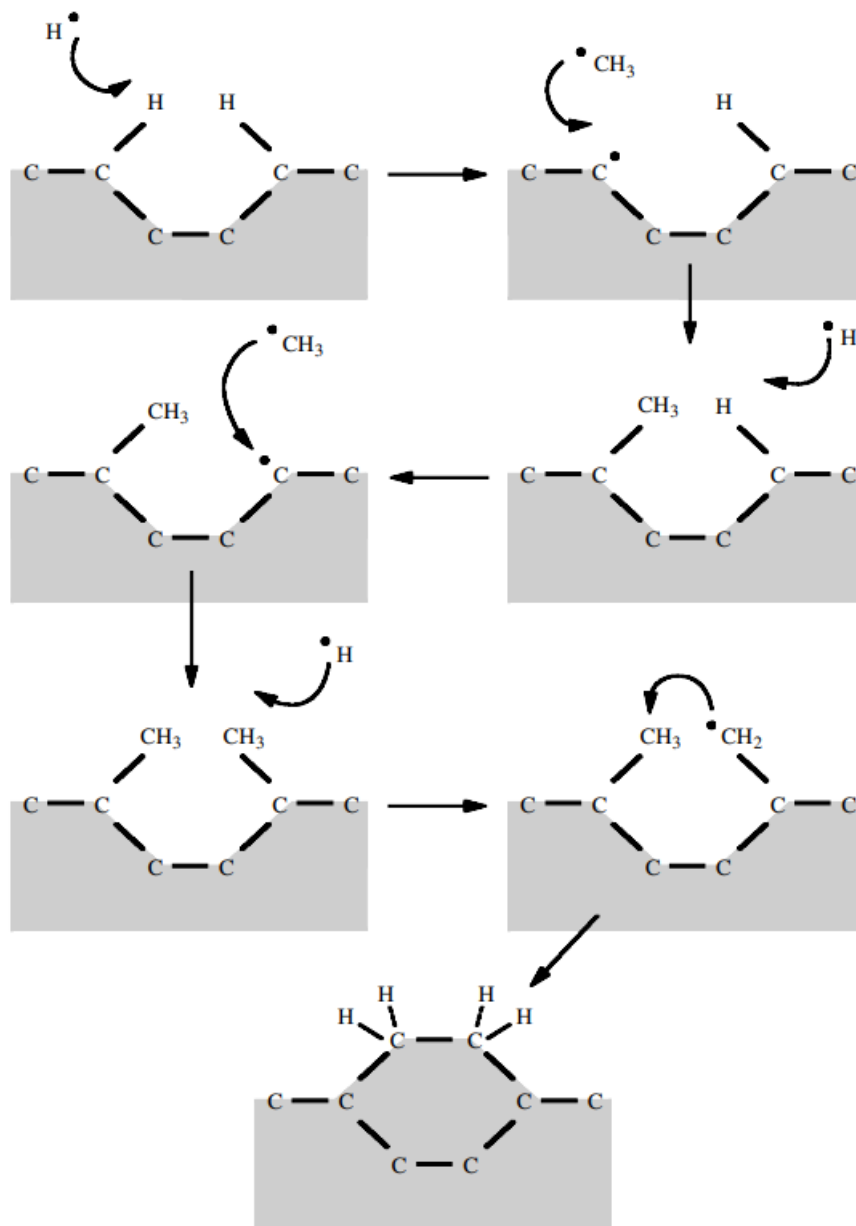


**Figure 4:** Simplified schematic diagram of the surface chemistry of diamond deposition. Reproduced from [14]

During deposition, the substrate surface temperature is 700-1400 °C<sup>19</sup>, however some specific reactors discussed later can have lower temperatures. The main reason for the high temperature is to maintain a good rate of growth while still favouring diamond production over graphite<sup>19</sup>.

Inducing diamond nucleation on non-diamond substrates is very difficult and requires the assistances of bias enhanced nucleation (BEN)<sup>23</sup>. BEN can be used in HFCVD (section 4.1.3) and MPCVD. In both cases a voltage is applied to the reactant gases, creating positively charged ions. A negative voltage is applied to the substrate surface, and Coulombic attraction then aids growth. However, the

charge also increases the force of nucleation, causing surface damage which produces lower quality diamond films.

### **3.2.5 Newly Proposed Diamond Growth Mechanism**

Recently an alternative mechanism to the sequential build-up of  $sp^3$  layers has been proposed in which graphite is thought to spontaneously transform into diamond<sup>24</sup>. Using *In situ* direct monitoring, the diamond growth process was observed by high resolution transmission electron microscopy (HRTEM) and Raman spectroscopy. Results showed five observed stages; (i) No growth (NCD seeds), (ii) a graphene film growing on the surface, (iii) vertical sheets of graphene, (iv) large graphite nano-rods, (v) NCD film and disordered graphite. HRTEM images show with greater deposition the stage (iii) vertical graphene sheets transition into the phase (iv) graphite nano-rods. From stage (iv) it should be noted the study indicates the nano-rods ‘probably’ and not conclusively transform into stage (v) NCD film (figure 5). However, the model is additionally supported by the absence of graphite nano-rods in the stage (v) sample and the presence of rod like diamond formation.

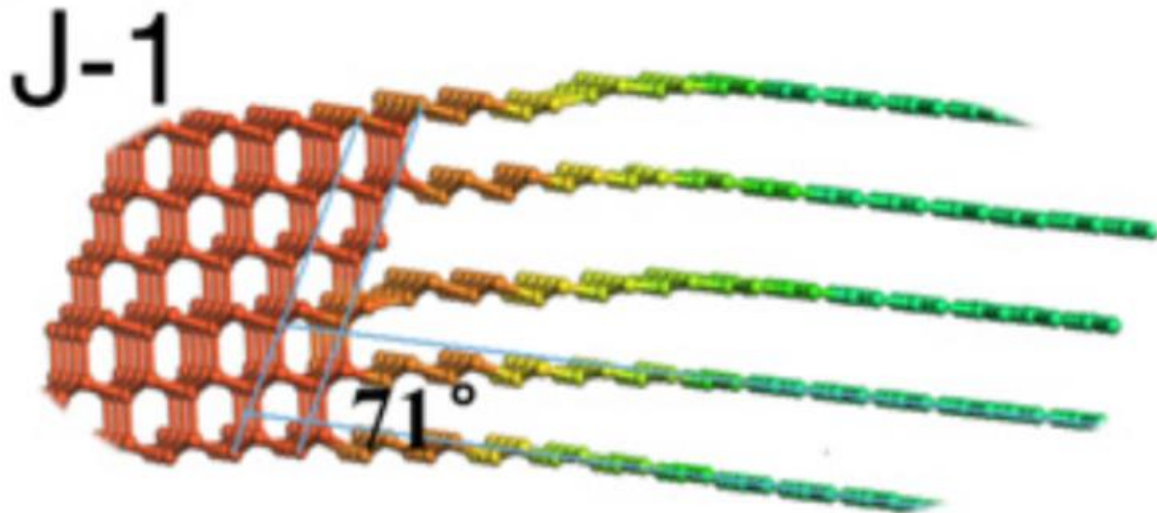


**Figure 5:** Sketch of the phase transformation (orange) from graphite (green) to diamond (red) in the graphite needle grown on NCD seed. Graphite needles grow  $71^\circ$  from the diamond plane. Reproduced from [24]

Computational modelling also indicated the presence of atomic Ta in HFCVD, which was shown to catalyse the spontaneous conversion in both O and H terminated diamond. In the absence of Ta, H was deemed essential for conversion which is in line with current understanding of CVD growth.

### 3.3 Reactor Types

#### 3.3.1 Hot Filament CVD

Hot filament CVD (HFCVD) uses high temperature (2000-3000 °C) metal filaments to activate gaseous species into radicals<sup>25-28</sup>. Filaments are arranged in rows covering the substrate deposition area (figure 6).

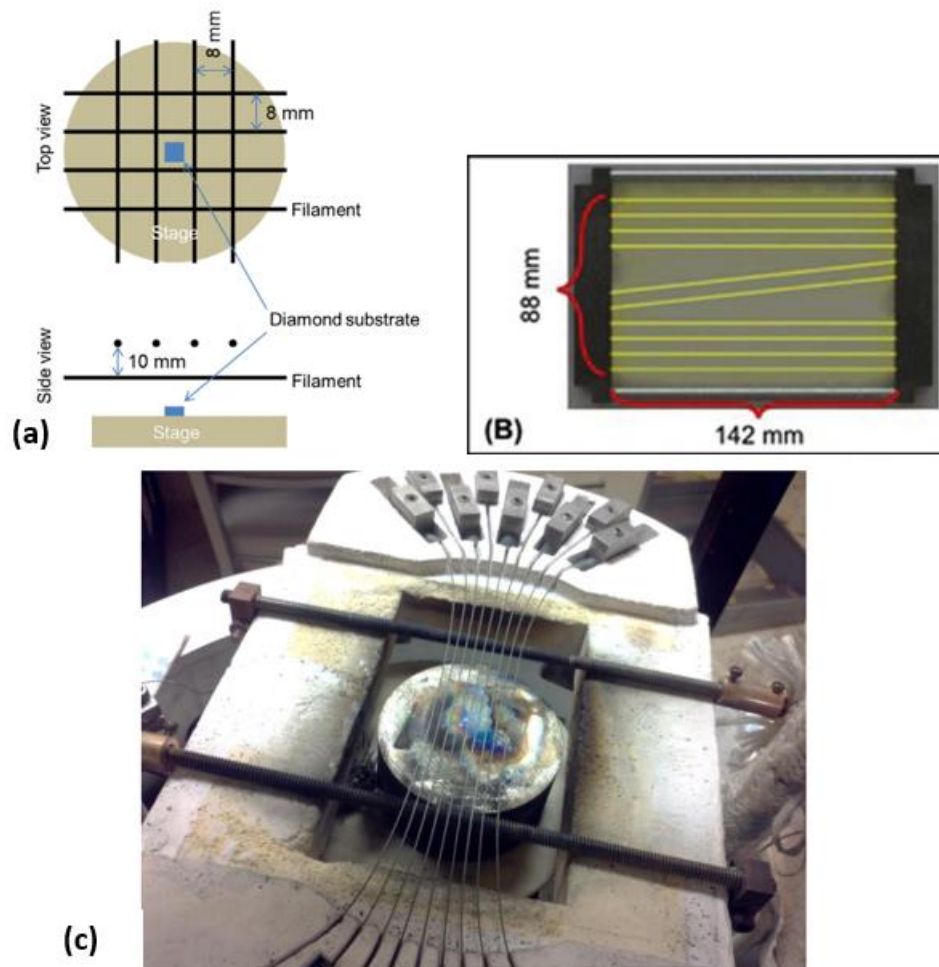


**Figure 6:** (a) Top and side view from a two layer filament arrangement<sup>28</sup> (b) Top view of a one-layer filament arrangement<sup>29</sup> (c) One layer W filament arrangement<sup>27</sup>

Reactors operate at low pressures of 2-8 kPa with controlled gas flow, typically  $H_2/CH_4$  are continually fed at 100/2 sccm. The substrate is heated to typically 700 – 1100 °C by conduction of filament heat, and kept uniform *via* backside water cooling or additional heating<sup>14, 27, 28</sup>. Once the gas is activated, radical species diffuse toward the substrate where deposition occurs. A general reactor schematic diagram is shown in figure 7.

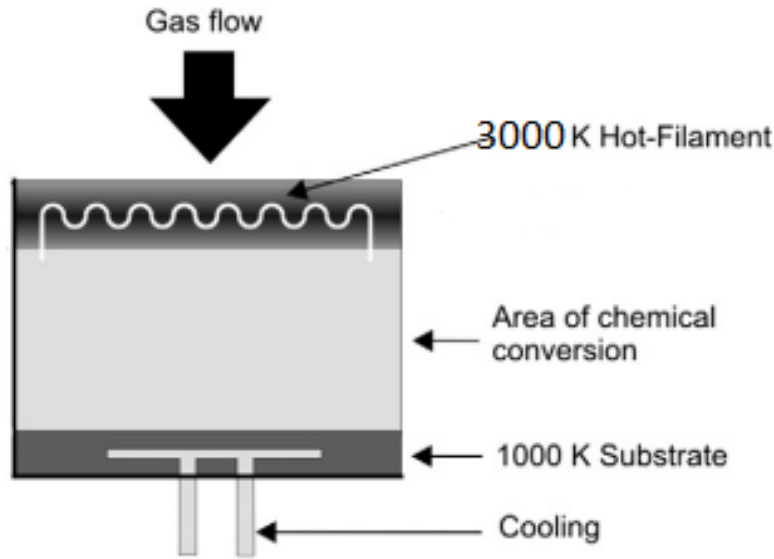


**Figure 7:** Representation of a hot Filament CVD reactor. Adapted from [19]

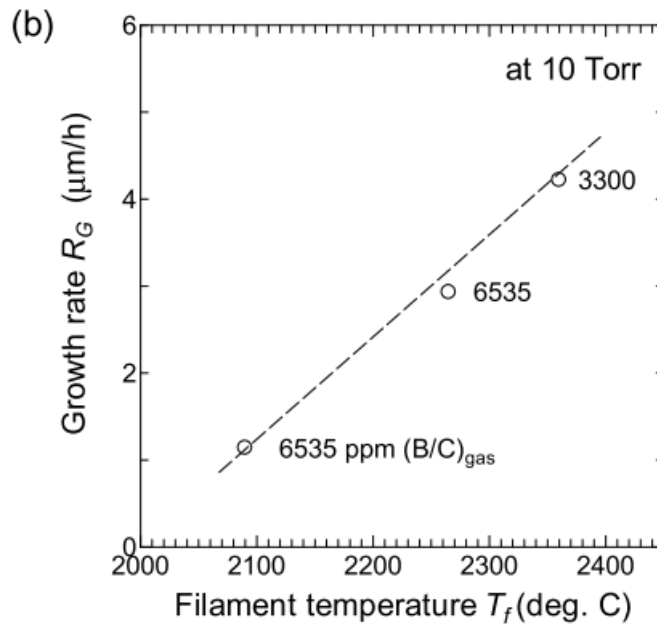


**Figure 8:** Filament temperature ( $T_f$ ) at a fixed gas ratio and identical setup. Reproduced from [30]

The diamond growth rate increases with high filament temperatures (figure 8). For enhanced growth rates the temperature must be as high as possible. Commonly tungsten (W) and tantalum (Ta) are used as their high melting points allow them to survive. However, the temperature and exposure to a carbon environment for an extended period of time causes carburisation (formation of a carbide) of filaments<sup>27, 28, 31</sup>. Some systems incorporate this *via* a dry run (no substrate) to carburise, and then using the high melting points of the carbides (W, 2875°C and Ta, 3880°C) to enable higher temperatures/growth rate during a later growth run.

HFCVD is relatively cheap and is capable of producing: polycrystalline, microcrystalline, nanocrystalline, ultra-nanocrystalline and single-crystal diamond<sup>28, 32</sup>. However, despite pre-

carburisation, eventually the filament will degrade leading to metal impurities in the diamond lattice, degrading electronic capabilities<sup>3, 4, 9</sup>.

### 3.3.2 Microwave Plasma CVD

Microwave plasma CVD (MPCVD) uses a microwave generator (usually 2.45 GHz or 915 MHz) and wave guides to create resonance in a resonance cavity<sup>33-36</sup>. Reactors are designed to then create a plasma through the ignition of feed gases via the discharge from the microwave resonance and quartz window<sup>14</sup> (figure 9). The plasma is designed to concentrate its density on the substrate<sup>33</sup>. Reactors operate at higher pressures (5–14 kPa)<sup>33-35</sup> than HFCVD. Due to the pressure, radicals cannot diffuse toward a substrate, hence the plasma is required<sup>33</sup>. The gas phase reactions also differ slightly from HFCVD as the atomic H is not produced by electronic dissociation, but rather thermal decomposition<sup>33</sup>. This is due to the increased pressure and very high temperature plasma.

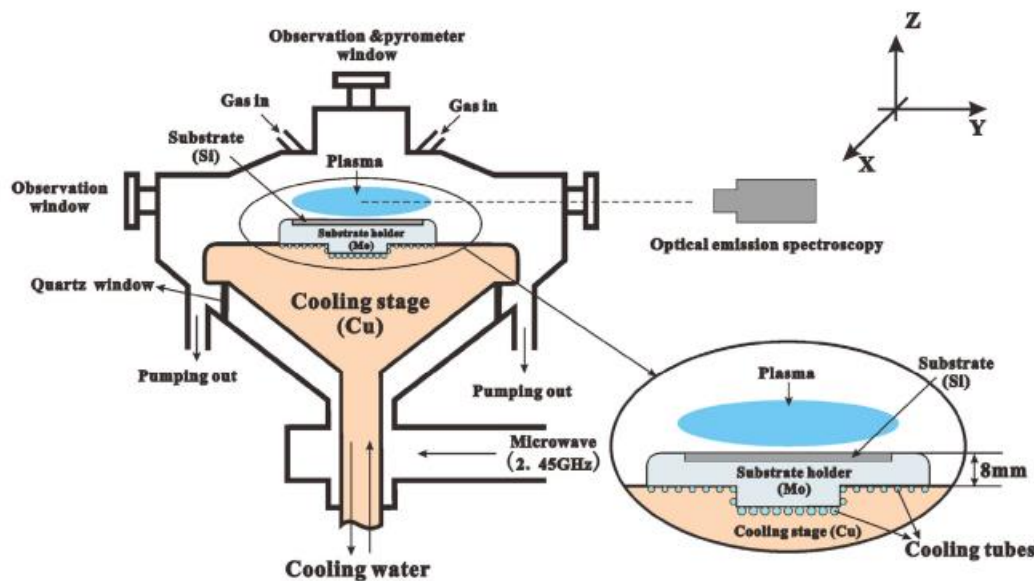


Figure 9: Schematic diagram of a MPCVD reactor<sup>37</sup>

The microwave power controls the surface temperature by conduction, which in turn, influences the diamond quality and grain size<sup>33, 38</sup>. Increasing the surface temperature (by increased microwave power) raises the energy of adsorbed particles, which increases the rate of surface reactions. At higher temperatures radical species are created in the plasma increasing the rate of etching and diamond growth rate. Both factors contribute to increased diamond growth.

The temperature across a substrate affects the uniformity of growth rates<sup>39</sup>. Unequal heating can create areas of higher temperature where growth rate increases compared to cooler regions. For SCD uniformity the substrate temperature must be kept consistent using a method such as backside cooling.

### 3.3.3 Point-Arc Remote Plasma CVD

Point arc remote plasma CVD operates similarly to MPCVD however only one antenna is used to ignite a small plasma ball at the tip for small area CVD diamond growth (figure 10)<sup>40</sup>. The technique was developed to create ultra-pure patterned diamond for electronic applications. This is done by depositing a SiO<sub>2</sub> mask on a diamond seed substrate and etching a pattern *via* inductive-coupled plasma-ion reactive etching (ICP-RIE) and lift off process. The small-scale CVD deposition is then

carried out, growing the patterned diamond. Once deposition is complete the SiO<sub>2</sub> mask is then chemically removed.

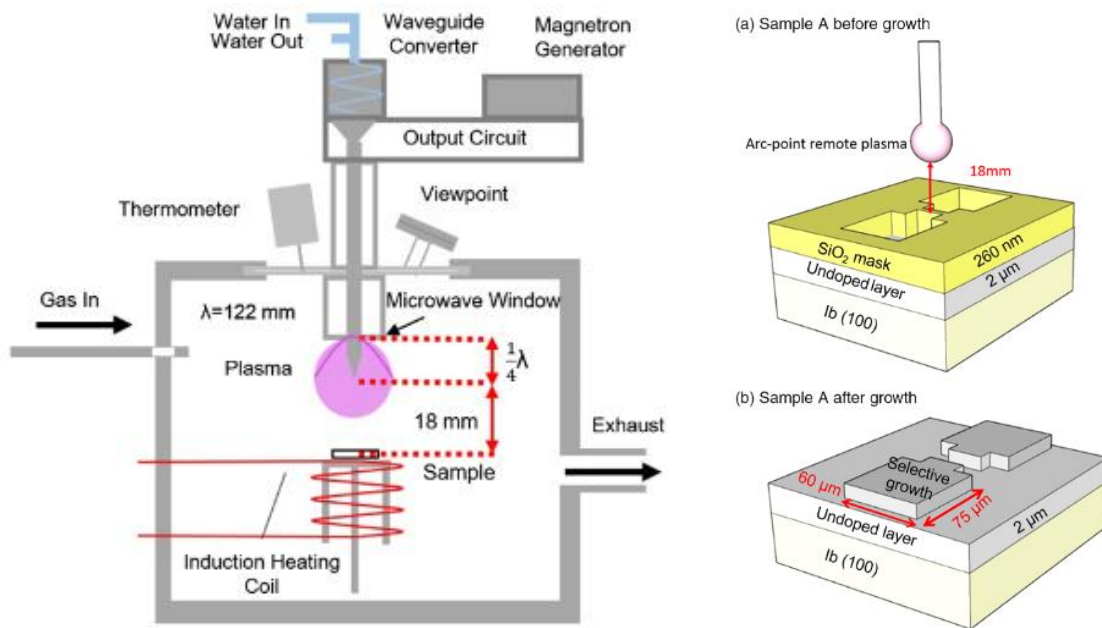


**Figure 10:** (left) Schematic diagram of a point-arc remote MPCVD reactor.(right)(a) Before selective growth with a 260 nm SiO<sub>2</sub> mask (b) After 4h selective growth and chemical removal of mask. Figure reproduced from [40]

### **3.4 Large Area CVD**

#### **3.4.1 Upscaling HFCVD**

##### **3.4.1.1 Activation**

The activation stage of a HFCVD reactor can be upscaled by increasing the number of filaments used<sup>27</sup>. The deposition requires full coverage of a substrate. Provided a large enough seeded substrate is used, there is no limit to the area which can be covered by increasing the number of filaments. Currently commercial reactors such as NeoCoat's CVDiam HF 120 can deposit over areas of 400 × 1180 mm<sup>41</sup>.

##### **3.4.1.2 Gas Composition**

In HFCVD there are several different film grain sizes that can form by altering the gas ratios; Microcrystalline (grain size  $\leq 1 \mu\text{m}$ ), Nanocrystalline (NCD)(grain size  $\approx 6 - 100 \text{ nm}$ ) and Ultra-nanocrystalline (UNCD)(3-7 nm)<sup>32</sup>. An Ar rich ratio of Ar/H<sub>2</sub>/CH<sub>4</sub> in 70/30/2 sccm grows NCD with grain size 10-50 nm and a 90/10/2 sccm grows UNCD with grain size 3-7 nm<sup>32</sup>. The growth of smaller grain sizes is not without its caveats, as it reduces growth rates (249 nm h<sup>-1</sup> for NCD, 80 nm h<sup>-1</sup> for UNCD). UNCD is desirable as it has similar conductive properties to BDD and can be used in electronic applications<sup>42</sup>. It also has the most uniform thickness (approx. 5 % variance<sup>32</sup>) and least lattice strain, which helps prevent cracking, making it more desired for larger scale. Therefore, reactant tailoring is suited to applications where a thin high-quality film is required, such as doped diamond circuits.

##### **3.4.1.3 BEN-BEG**

To mitigate the low growth and thin film issues with UNCD and enable patterned growth (circuits), HFCVD can be paired with biased enhanced nucleation-biased to make enhanced growth (BEN-BEG)<sup>29</sup>. Here, positively charged ions are produced by positively biasing the filament, these then deposit on a negatively biased substrate, enhancing growth (figure 11).

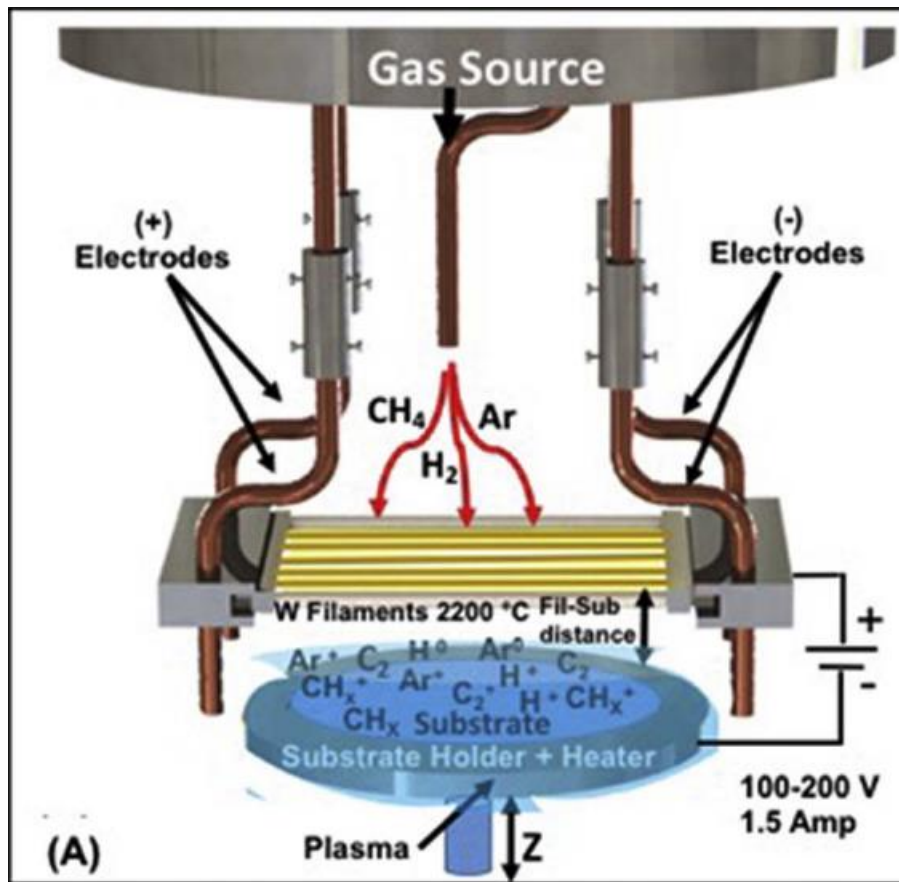


**Figure 11:** HFCVD reactor paired with BEN-BEG between the filaments and substrate, showing the production of positively charged ions for deposition on a negative Si substrate. Reproduced from [29]

It has been shown the optimal production of a functional UNCD diamond layer requires 2 hrs of BEN-BEG growth followed by 2 hrs of non-biased growth<sup>29</sup>. Due to enhanced ion bombardment and H etching, 2.5 hrs of BEN sees the destruction of UNCD film hence it must be removed for further growth. Using this technique, diamond films have been deposited on patterned Si substrates showing it can be paired with HFCVD to produce functional UNCD.

### **3.4.2 Upscaling MPCVD**

The main problem with upscaling MPCVD is enlarging the plasma to cover a large area whilst maintaining its uniformity and density<sup>33</sup>. Without an increase in power or pressure, simply enlarging the plasma area decreases its density to ineffective levels.

#### **3.4.2.1 Increased power and wavelength**

Using 15 kW quartz bell jar (figure 12) reactors operating at 915 MHz, microcrystalline (grain sizes 20-30  $\mu\text{m}$ ) quality PCD has been deposited on 100 mm substrates with a growth rate of 1  $\mu\text{m}^{18}$ . UNCD has been grown over even larger areas (200 mm) in a 7kW, 915 MHz reactor with thickness variance of 6% across the sample<sup>34</sup>. The power reduction reduces grain size but at the cost of growth rate (30-460  $\text{nm h}^{-1}$ ). Very high powered (75 kW) bell jar reactors have batch grown SCDs (up to 300) in even larger plasmas (300 mm), whilst maintaining uniform temperature distribution ( $\pm 250\text{ }^\circ\text{C}$ ) and good density<sup>43</sup>. However the growth rate of pure samples is unknown, as the reactor and samples were contaminated with N which increases growth rate but renders the crystals unusable for electronic applications. Increasing the power also raises the quality of diamond films due to increased plasma etching of deformities<sup>44</sup>.

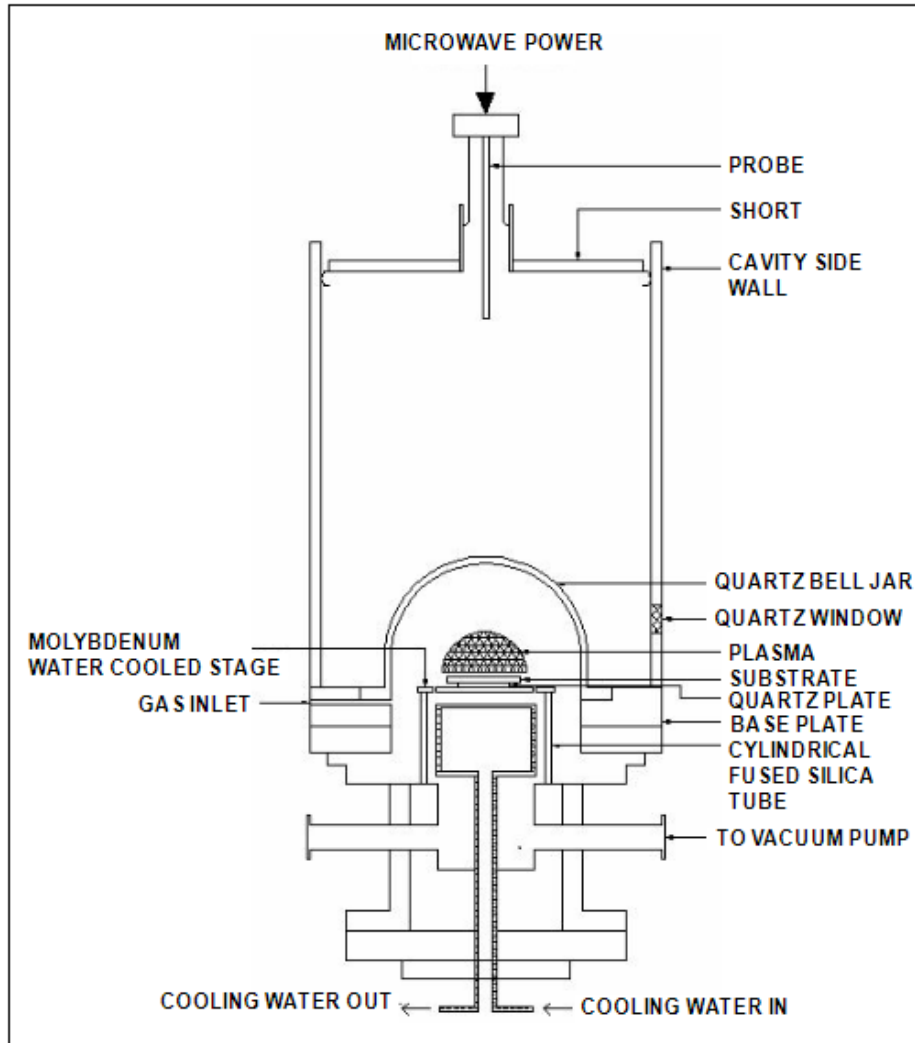


**Figure 12:** Schematic diagram of a 915 MHz quartz bell jar reactor. Reproduced from [18]

### **3.4.2.2 Increased Pressure**

Raising the internal pressure of a MPCVD system has been shown to increase growth and film quality<sup>33</sup>. It has been demonstrated that a 2.45 GHz reactor operating at higher pressure (30 kPa) can maintain plasma density and deposit diamond over a 75 mm area. But to maintain plasma at higher pressure requires higher MW again.

### **3.4.2.3 Multi-Mode Resonant Cavity MPCVD**

In a multi-mode MPCVD, the reactor has more than one microwave mode. This allows for multiple plasmas to be created which can overlap and cover larger areas. In a dual mode system powered by a 10 kW generator and operating at 2450 MHz a stable uniform plasma was grown to cover a 100 mm area<sup>45</sup>. Increasing the operational wavelength to 915 MHz saw further growth of a stable plasma area to 150 mm, however films produced were PCD (20-30  $\mu\text{m}$ )<sup>46</sup>.

### 3.4.2.4 DAA

An alternative solution for the scaling up of MPCVD is the use of a distributed antenna array (DAA). Instead of building a costly, large MPCVD reactor, DAAs incorporate multiple small plasma sources working together to cover a large area, an example of a  $4 \times 4$  reactor is shown in fig. 13a. DAAs operate low pressure ( $< 100$  Pa) and in the temperature range of  $130$ - $500$  °C<sup>47, 48</sup>. The low pressures prevent overheating of the substrate surface which favours diamond formation over graphite<sup>49</sup>. However, at low temperatures DAAs suffer from reduced growth rate ( $15$ - $17$  nm h<sup>-1</sup>). Using DAAs, NCD has been grown on heteroepitaxial substrates<sup>49</sup>.

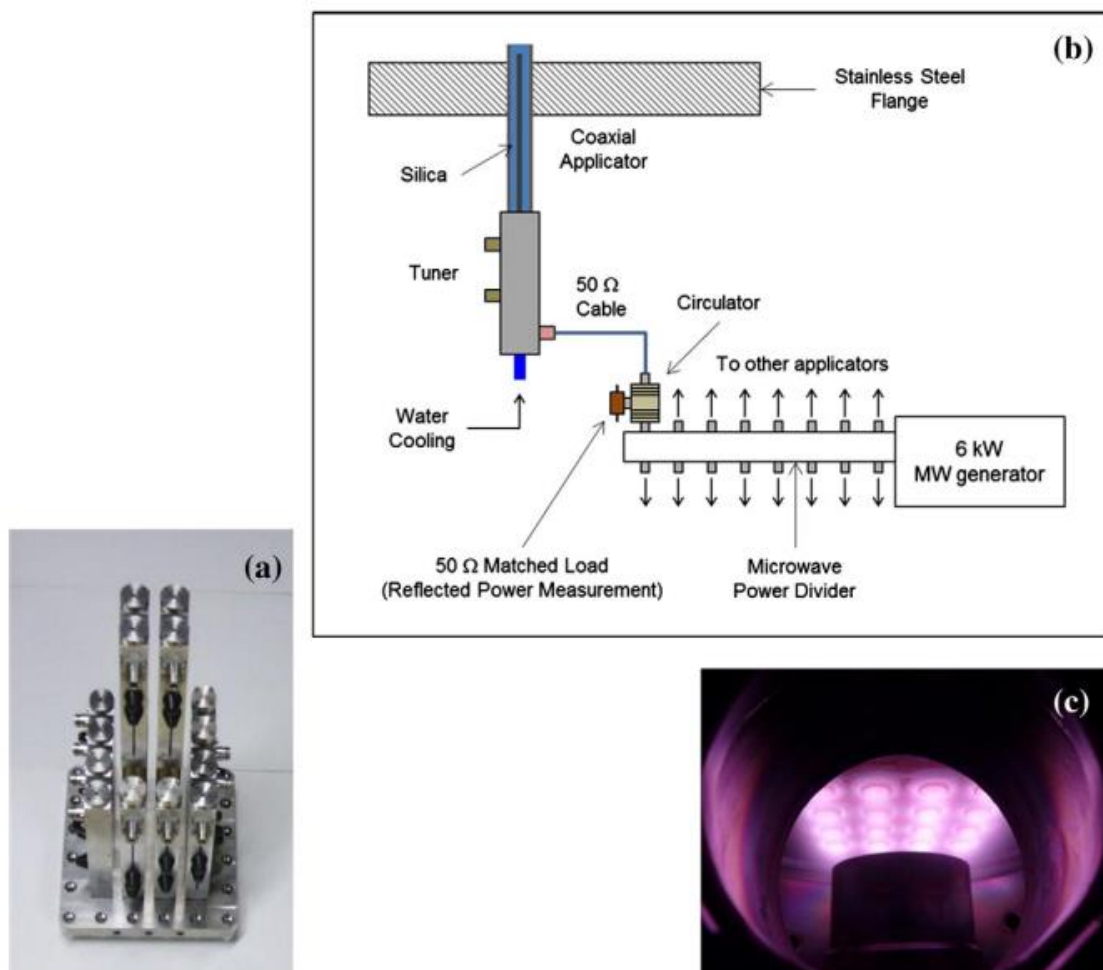


**Figure 13.** Figure reproduced from [47] (a) 16 coaxial plasma sources arranged in a square 2D-matrix (b) Design of a coaxial plasma source (c) View of ignited plasma sources inside the chamber.

As described by [47], in a DAA microwaves are generated from a central source, transported *via* antennas and guided into a power divider using a waveguide. The power is then separated equally and transported to each plasma source *via* a cable (figure 13b). Once powered each source is ignited creating a small, individual plasma bubble around itself, an example of which is shown in figure 13c. The microwave power is then increased, expanding the plasmas until they overlap, forming a ‘sheet of uniform plasma’<sup>47</sup>.

The low temperature operation has particular applications in heteroepitaxial coatings of substances with low melting points. One example would be the potential coating of the plastic polytetrafluoroethylene (PTFE), commonly used in medical implants, which has a melting temperature of  $330$  °C<sup>50, 51</sup>.

### 3.4.2.5 SWP

Surface wave plasma (SWP) CVD is a low temperature ( $\leq 400$  °C), low pressure (50 Pa), large area deposition technique in which a SWP is created by electromagnetic excitation<sup>52</sup>. Microwave power is essentially input from one source and spread out over a larger area, enlarging the plasma area. Previous iterations of SWP setups have used either linear or slotted antennae for excitation, however these suffered from a variety of issues culminating in non-uniform microwave power supply and uneven plasma distribution<sup>52-54</sup>. To mitigate these issues new systems were proposed for large area CVD that contain composite right and left hand (CRLH) wave guides (figure 14)<sup>52</sup>. The CRLH waveguides provide uninterrupted microwave transmission to the resonant launcher section, where a large uniform surface current is then induced. The current then induces a SWP in the CVD reaction chamber enabling diamond growth. Using CRLH SWP MPCVD, and a reactor operating at 2.465 GHz, NCD films have been grown over large areas (100 mm). Due to the low temperature operation, SWP is also applicable for coating substrates with low melting temperatures.

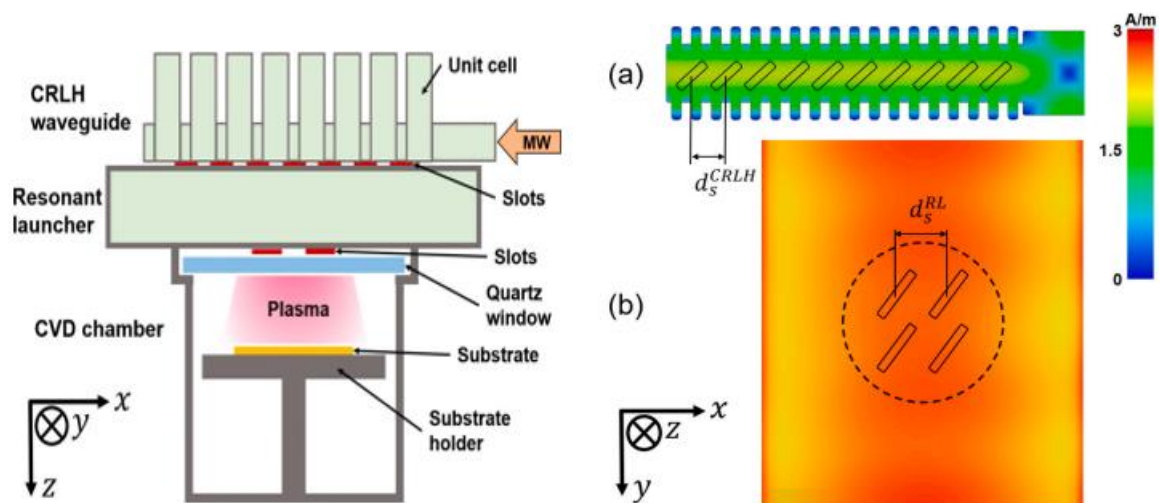


**Figure 14:** Figure reproduced from [52]. (Left) Schematic diagram of a SWP MPCVD system, consisting of composite right and left hand (CRLH) waveguide section, the resonant launcher and CVD chamber. (a) Surface current density on CRLH waveguide. (b) Surface current density on the resonant launcher. Dashed black line represents quartz window, black rectangles represent excitation slots.

### 3.4.2.6 Gas Composition

Similarly to HFCVD, the introduction of Ar to the gas composition MPCVD increases diamond growth and quality whilst reducing lattice strain for larger area growth<sup>37</sup>. However, at high microwave power the Ar increases the  $e^-$  electron density of the plasma, which has a detrimental effect upon diamond growth and uniformity<sup>37</sup>. To mitigate this, a higher proportion of  $H_2$  gas is used in a ratio of Ar/ $H_2$ / $CH_4$ , 300/100/6 sccm.

### **3.4.3 Substrate Upscaling**

The size of the deposition area a reactor can produce is inconsequential if there is not a substrate seed large enough to facilitate the diamond growth. It is therefore vital to upscale the substrates used.

#### **3.4.3.1 Seed Recovery**

The ability to recover a seed is critical to upscaling. SCD growth requires expensive high quality crystal seed substrates (usually type 1b HPHT diamond<sup>55</sup>). A process which doesn't allow for the recovery of these seeds is not economically favourable, a factor that increases for larger scale SCD growth requiring larger seeds.

Using laser recovery on  $3.5 \times 3.5 \text{ mm}^2$  (1.4 mm thick) seed crystal, allowed for their use in 20 growth cycles<sup>56</sup>. In this method, the grown diamond and seed are sliced apart by laser cutting in their interlayer. The substrate is then thermo-mechanically polished to remove surface damage (removing 20-50  $\mu\text{m}$  from the seed). A further laser cutting is then used to remove polycrystalline diamond from the edge of the seed. The seed can then be reused. Eventually the seed becomes too thin for recovery, however its lifetime is significantly extended compared to that of non-recoverable seeds. The process may be unsuitable for ultra-thin diamond growth because of material loss due to the laser beam thickness (20  $\mu\text{m}$ ).

#### **3.4.3.2 Mosaicing**

Mosaic growth is a form of homoepitaxial CVD in which many diamond seed plates are arranged in a grid and grown laterally, fusing them together. The resultant wafer is formed of small tiles, hence the name mosaic growth<sup>57</sup>.

There is lattice strain within mosaic wafers. Raman peak-shift mapping has shown localised strain along crystal boundaries (CB), but no tensile and compression stress near the CB<sup>25</sup>, indicating the major strain of mosaic wafers is within the boundary and no additional stress is put on the precursor crystals. The maximum stress in the CBs was comparable to the compression (-93 MPa)<sup>58</sup> and tensile (+40 MPa)<sup>58</sup> stress of SCD dislocations (figure 15c) and an order of magnitude lower than PCD<sup>25</sup>. However large (200  $\mu\text{m}$ ) CBs increase the defect density, shown in figure 15d by the increased red area. Therefore, the maximum stress of an individual defect may be similar to SCD, but large boundaries increase the number of points of stress, weakening the overall wafer. The boundaries also make the crystals unsuitable for semiconductor applications. Even if each tile were appropriately doped, the defects make the boundaries electrically insulating<sup>25</sup>.

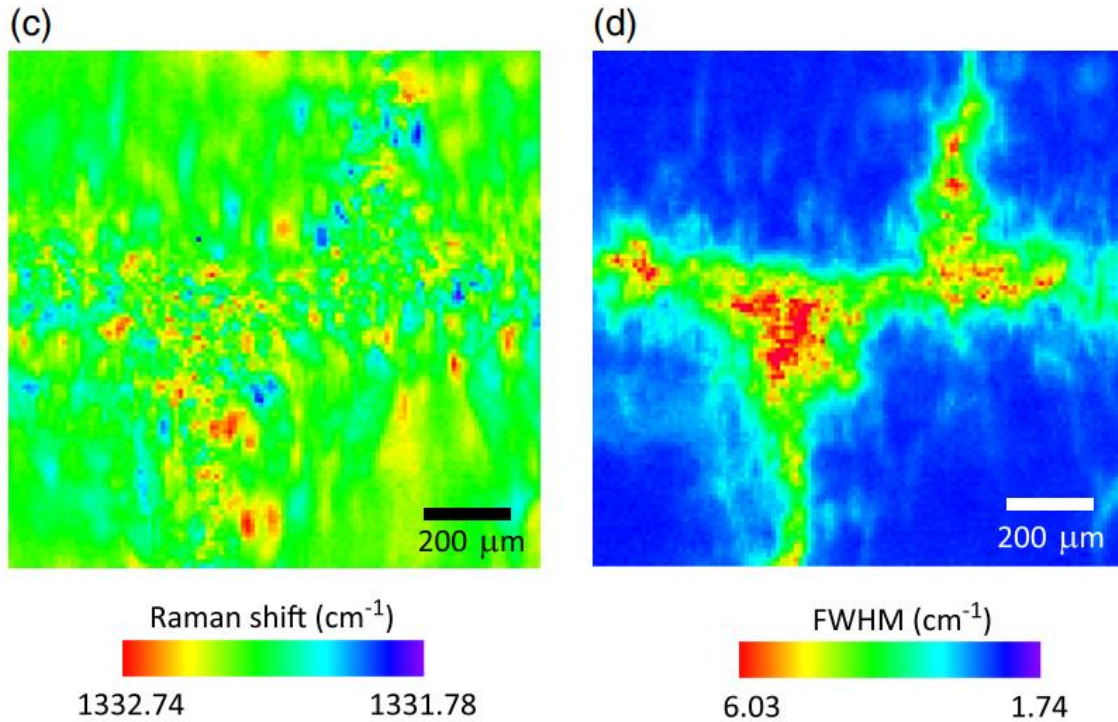


**Figure 15:** (c) Mosaic wafer Raman shift, depicting points of maximum stress (red and blue) (d) Full width at half maximum, depicting the high defect density (red areas) inside CBs. Reproduced from [25]

Due to the importance of the strength and SCD structure to the applications of a diamond wafer, internal strain must be minimised, therefore, the size of boundaries must be reduced. This requires plates to be aligned accurately and have identical off axis orientation<sup>59</sup>. One method to achieve this is the use of cloned tiles (figure 16). The technique uses a lift-off method, in which a high energy ion beam implants a non-diamond layer on a substrate surface<sup>60</sup>. SCD plates are then grown via MPCVD and removed by electrochemical etching of the non-diamond layer. This allows for repeated growth (clones) of SCD plates that have the same characteristics. These can then be aligned and grown into a tiled clone<sup>59</sup>. Tiled clones still contain CBs but they can be used as a large-area seed crystal for homoepitaxial growth (figure 16). The clone is mechanically polished for a uniform surface, then ion implanted for the lift-off process. Using this method, wafers of  $20 \times 40\text{mm}^2$  and  $60 \times 40 \text{mm}^2$  have been produced<sup>61, 62</sup>. However, it was noted that non-uniform temperature across the substrate caused variable impurity concentration across the plates produced. It may be beneficial to combine the technique with substrate backside cooling used in other CVD<sup>27</sup> methods to maintain uniform temperatures.

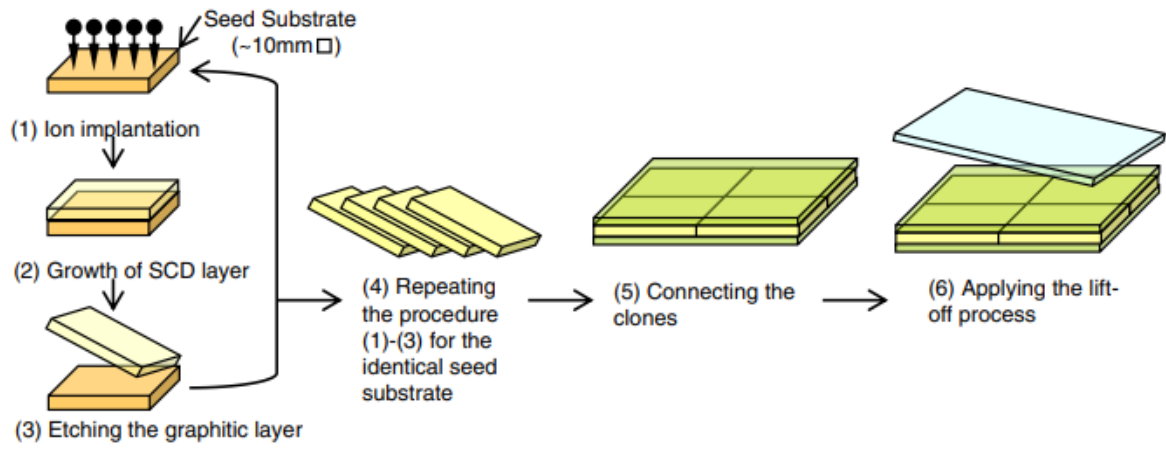


**Figure 16:** Procedure to produce clones and tiled clones. Figure reproduced from [59]

### 3.5 Project Context

During the project, the commissioning of a larger area hot filament CVD reactor has been undertaken. The reactor will be used to grow high surface area diamond electron stripper plates for the ISIS Neutron and Muon Source (**Figure 17**), replacing the current generation of aluminium oxide stripping foil.



**Figure 17:** Illustration schematic of the ISIS facility. Reproduced from [63]

The ISIS Neutron and Muon Source (**Figure 17**) is in practice a ‘super-microscope’<sup>64</sup>. It uses beams of neutrons to view the position of atoms and measure the forces acting between them. The ISIS laser uses an ion source to produce H<sup>-</sup> ions; these are then accelerated through a radio frequency quadrupole (RFQ), Linac high powered radio-frequency accelerator and finally a ten dipole synchrotron where they are accelerated up to 84% the speed of light<sup>65</sup>. As the beam is injected into the synchrotron the electrons are stripped off the H<sup>-</sup> ions by passing the beam through a 0.3 μm thick aluminium-oxide foil, producing a high energy proton beam (**Figure 18**). The beam is fired at carbon targets producing muons before then being fired at neutron targets.

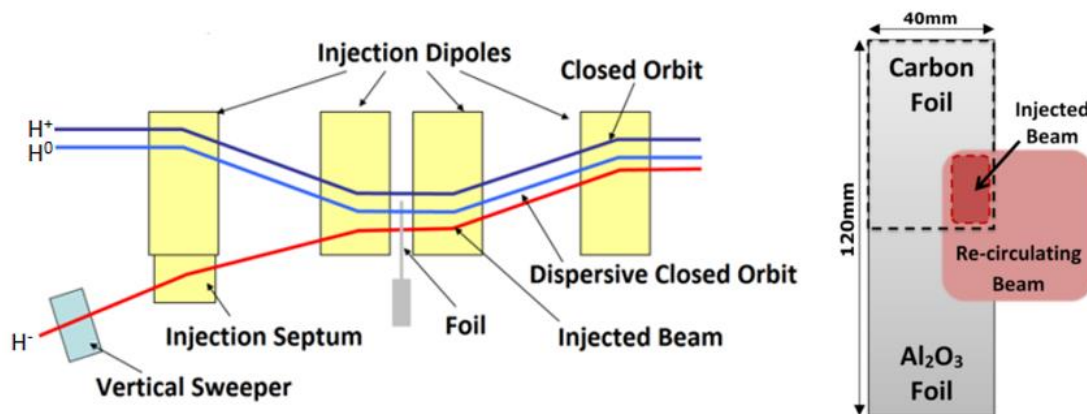


**Figure 18:** (Left) Schematic diagram of the ISIS  $H^-$  injection into the 800 MeV synchrotron through an electron-stripping foil. (Right) ISIS injection foils schematic. Reproduced from [66]

The original aluminium oxide foils were manufactured internally at ISIS. The process is highly complex and there are several stages of annealing, etching and coating (**Figure 19**)<sup>67</sup>. The process exceeded 20 h and had a high failure rate during installation<sup>66</sup>. Once installed however, the foils performed well and generally had life-times exceeding the average laser use cycle.

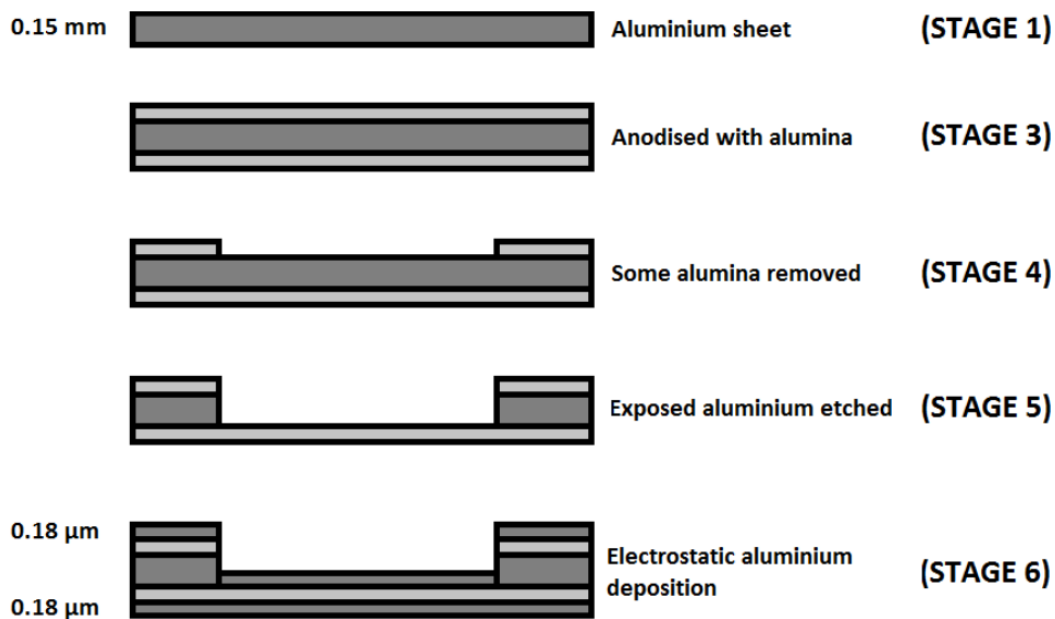


**Figure 19:** Schematic diagram of the production of the ISIS stripping foil through the stages of production. Reproduced from [67]

In 2010 the injection energy from the Linac to the synchrotron was upgraded from 180 MeV to 400 MeV<sup>68</sup>. As a consequence the 0.3 μm aluminium oxide foils had to be replaced as they could not survive the increased power and temperature. Thicker foils increased beam scattering to unacceptable levels (> 99 %), so these were not a viable alternative. To replace the aluminium foils, diamond like carbon (DLC) was chosen due to its superior stripping efficiency<sup>12</sup> and successful use at other facilities<sup>68</sup>.

The DLC foils were designed to be smaller so as to cover the injection point only (**Figure 18**). This reduced the unnecessary contact between the recirculating beam and the foil, reducing scattering and increasing efficiency. However, the loss of structural stability meant the foils performed poorly (efficiency < 40 %) due to deformation (**Figure 20**)<sup>66</sup>. Carbon-fibre supports were added to increase stability, however, fibres thick enough to sufficiently support the foil increased scattering to unacceptable levels. The fragility of the DLC meant they needed more frequent replacement, a costly and time consuming process. It also carries a radiation risk with typical film disposal requiring exposure to 20-100  $\mu\text{Sv}$  per foil change<sup>66</sup>.

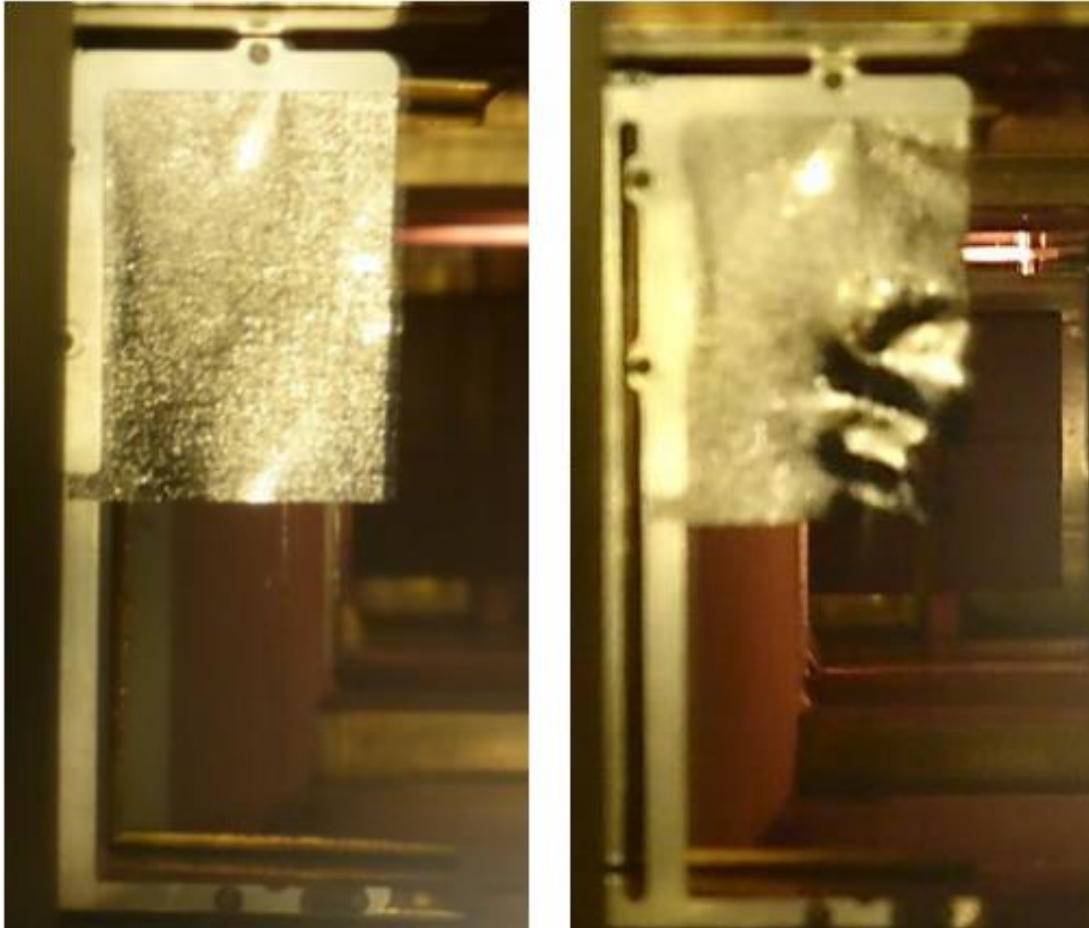


**Figure 20:** Diamond Like Carbon (DLC) foil installed in the ISIS synchrotron injection site. (Left) Newly installed (Right) After 17 h of operation. Reproduced from [66]

The next generation foils were made from nano-diamond and were fabricated by the Spallation Neutron Source (SNS) at ORNL, Tennessee. These thin films were designed to be supported on one edge whilst being able to withstand the energy of a 1.0 GeV beam<sup>69</sup> – exceeding the power requirements for the ISIS beam. The SNS foils were grown on a Si substrate (area 10 mm  $\times$  16 mm, **Figure 21**) patterned by photolithography<sup>69</sup>. A U-shaped corrugation pattern (**Figure 21**) was used to enhance the mechanical strength and prevent curling up under stress. The Si was seeded by ultrasonic scratching using a diamond abrasive slurry, to achieve a high nucleation density preventing pinhole gaps in the thin foil<sup>69</sup>. The diamond was grown in a 2.45 GHz MWPE CVD (1300 W, 50 Torr), with a 1/49/50 by volume  $\text{CH}_4/\text{H}_2/\text{Ar}$  gas composition, to uniform 1  $\mu\text{m}$  nano-diamond layer<sup>69, 70</sup>. The Si was chemically etched leaving a free standing diamond, bar one edge where the Si remains as a mechanical support.

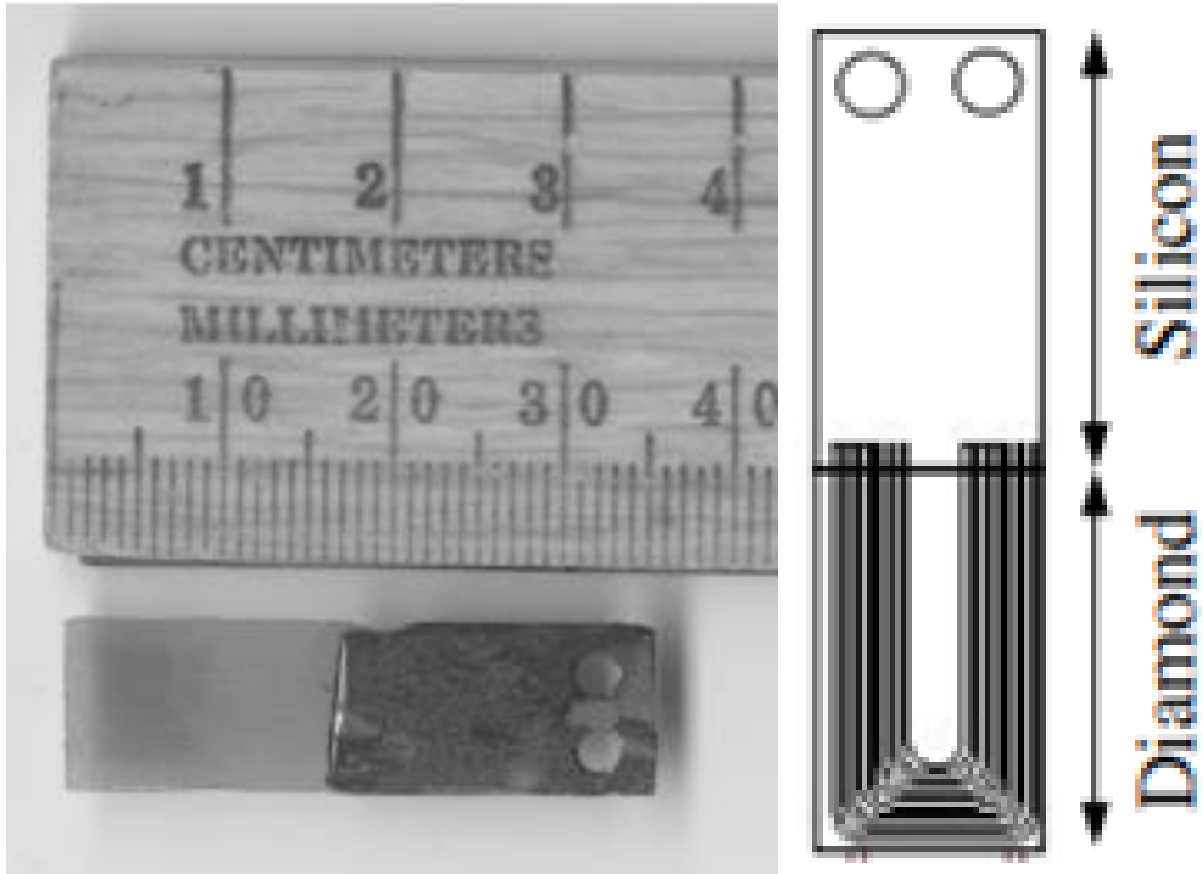


**Figure 21:** (Left) Corrugated diamond foil (area 10 mm × 16 mm), supported on one edge by Si substrate. (Right) Diagram of U-shaped corrugated support with 25 lines inch<sup>-1</sup>, 2mm curvature and 60 % substrate coverage. Reproduced from [69].

SNS were able to manufacture diamond foils to the size specification required for the ISIS reactor (55 mm × 30 mm), and were successfully used at ISIS for several years. However, SNS have since ceased making and supplying these films, and so ISIS is now looking for a new supplier. The Bristol Diamond Group was selected to grow the diamond foils in the large area HF CVD reactor.

## **4. Experimental Method**

### **4.1 Experimental Aims**

The aim of the literature review was to explore the problems associated with various large area CVD diamond growth techniques and solutions developed to overcome them.

The primary aim of the research was to commission the Bristol Diamond Group's large area CVD reactor (nicknamed "the toaster", or "the reactor formerly known as Thomas"). The secondary aim was to grow diamond foils for the ISIS neutron and muon source (**Section 3.5**) to the required specifications for use in the accelerator facility. The specifications were to make diamond plates of micro- to nanometre grain size, a 1  $\mu\text{m}$  thick film with no pinholes, over an area of  $30 \times 55$  mm.

To commission the reactor, diamond was grown on nanodiamond-seeded test Si plates, denoted TSX (where X represents sample number), using scaled-up growth conditions from a smaller hot filament reactor<sup>69-71</sup>. The test plates also served as trial samples to establish growth and seeding conditions for the ISIS samples. The reactor and techniques were then used to fabricate samples for ISIS, denoted ISX.

### **4.2 Samples**

The test samples were grown on  $30 \times 50$  mm silicon plates cut from a 6 inch silicon wafer (purchased from Silicon Materials, Type/Orient: N/Phos <100>) using a diamond scribe. The polished surface was scored vertically down the sample (**Figure 22**) using a diamond scribe to emulate a 3D corrugated surface. The ISIS samples were grown on  $30 \times 55$  mm patterned silicon plates (**Figure 22**) provided by the ISIS neutron and muon source.

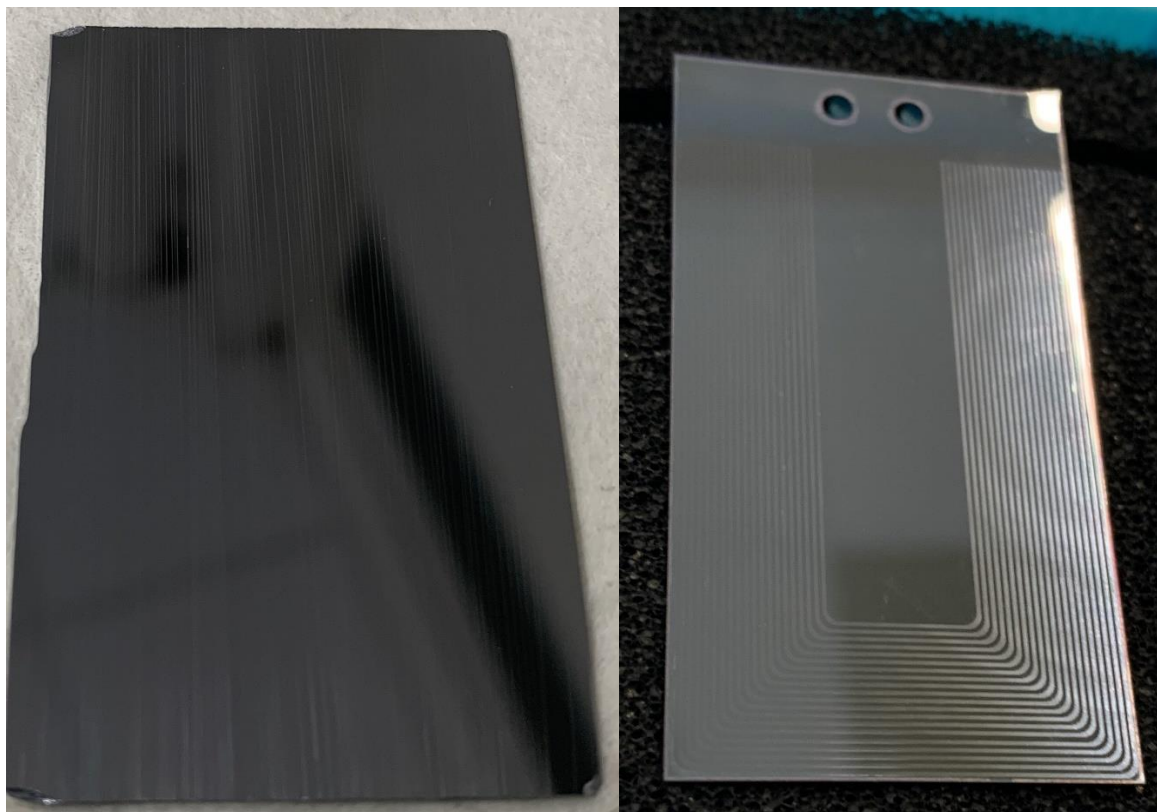


**Figure 22:** (Left) Vertically scored  $30 \times 50$  mm test Si plate. (Right)  $30 \times 55$  mm corrugated ISIS Si plate.

### 4.3 Seeding

The substrates were seeded with nano-diamond *via* ultrasonic dip seeding to provide nucleation sites for diamond growth. Dip seeding was selected to uniformly seed the 3D corrugated surface of the ISIS samples.

The seeding solution was made up by mixing 10 droplets of NanoAmando Colloid (purchased from NanoCarbon Research Institute Ltd., catalogue number: ND64/ 160-01, nanodiamond dispersion in water, particle size:  $3.3 \pm 0.6$  nm) in 28 ml methanol. The suspension was then subjected to ultrasound (using a Bandelin Sonoplus HD 2070, 40 % power, 3 h)(**Figure 23**) to homogenize and break up diamond aggregates. Immediately before each seeding, the solution was re-subjected to ultrasound (15 minutes).

The Si samples were submerged face-up in the solution. Single-seeded samples were submerged for 1 h, double-seeded samples were removed from the solution and dried, then resubmerged for an additional 1 h. After seeding, the samples were dried with a compressed air gun to prevent diamond clumps forming in pools on the surface.



**Figure 23:** Ultra-sound probe used to prepare the diamond seeding solution.

#### 4.4 Reactor Design

A modified large-area hot filament CVD reactor was used to grow the samples (**Figure 24**). The reactor casing was a stainless steel cylinder with a quartz side viewing window. The reactor walls were cooled by chilled (21 °C) water pipes, mounted to the lid. The reactor ran under continuous gas flow conditions with an operational pressure of 20 Torr. Mass flow controllers were used to set and monitor the gas flows during growth runs.



**Figure 24:** Modified large-area hot filament CVD reactor. (Left) The reactor control panel with pressure gauge, mass flow controllers and filament power controls. (Right) The stainless steel reactor casing.

Initially, the reactor was powered by a newly installed 210 A, 48 V DC, 10 kW power supply. However, due to an electrical problem the power supply was non-operational. Instead the reactor power reverted to the original 125 A, 24 V DC, 3 kW power supply for all growth runs.

Internally, the reactor (**Figure 25**) consisted of three stainless steel rods mounted to the reactor lid. The central rod was indented with mounting points which attached to the substrate-holder clamps, the filament-substrate distance was 4 mm. The power supply was connected through copper feedthroughs which attached to the rear two rods, which were connected in parallel through the filaments.

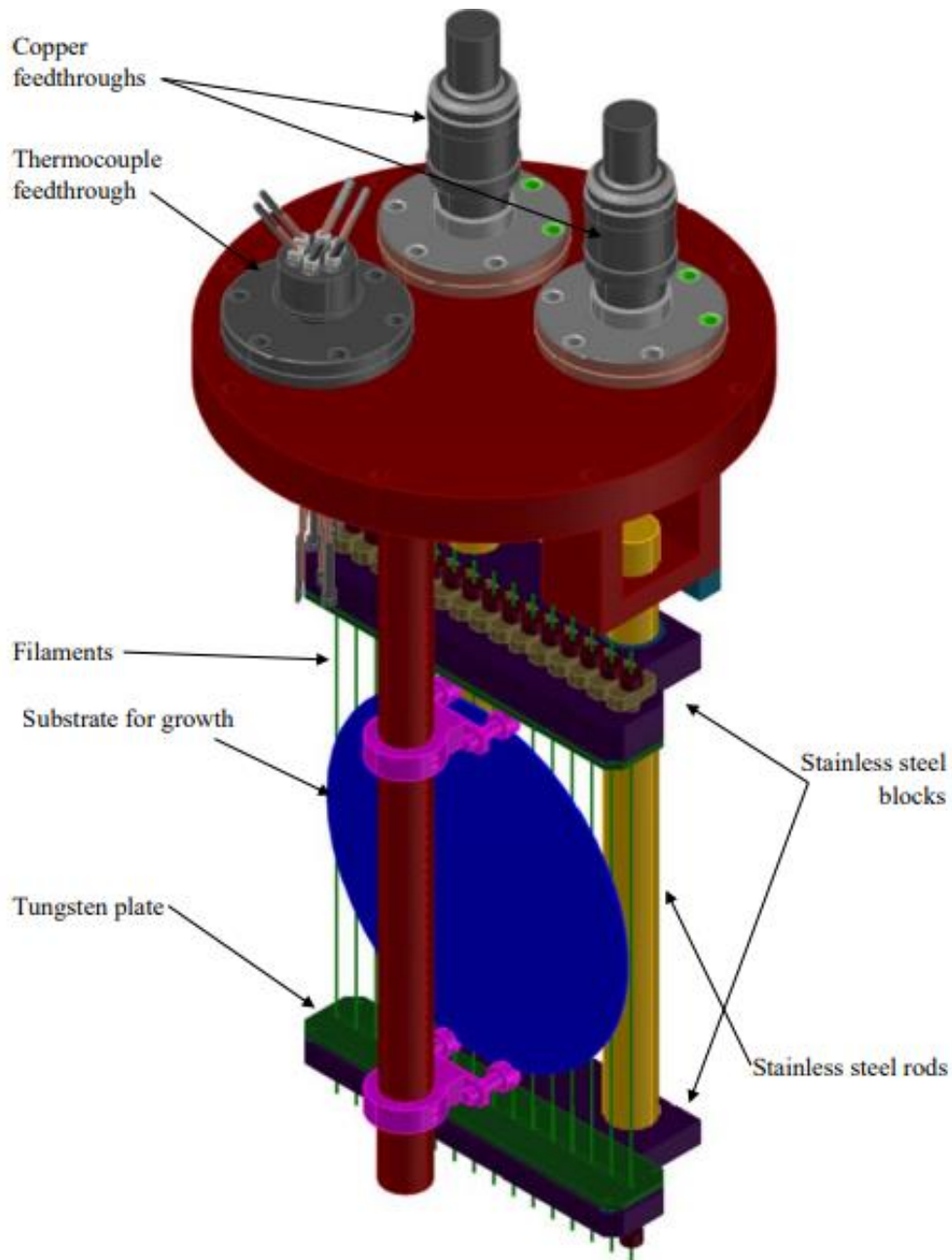


**Figure 25:** Figure reproduced from [71]. Large-area HF CVD reactor design. Pink: Adjustable stainless steel substrate holder clamps. Blue: A mounted Si wafer. Yellow: Stainless steel rods which allow flow of current into and out of the reactor. Green: Vertical filaments which form a circuit with the rods through W plates.

#### **4.5.1 Filament Arrangement**

3-4 Ta wire filaments (purchased from Advent Research Materials Ltd, Catalogue Number: TA550518, diameter 0.25 mm, length 7 cm, purity 99.9%) were arranged vertically with 10 mm spacing between them (**Figures 25 & 26**). The top end was bolted in place, with the lower end weighted to keep the filaments straight and taut when they expand due to heating. Tungsten plates were positioned above and below the sample (**Figures 25 & 25**) to ensure electrical contact with the filaments which prevented a short circuit.

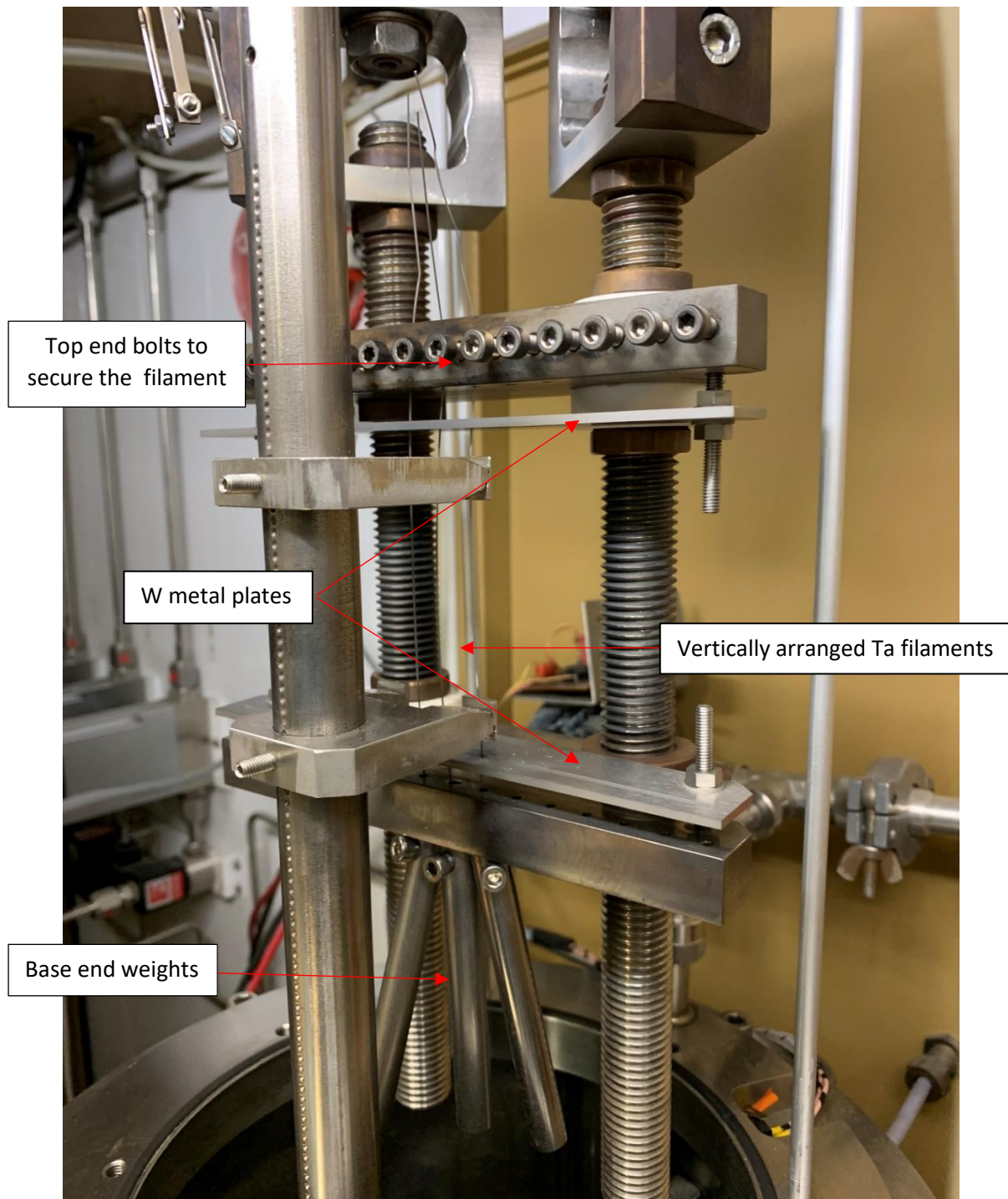


**Figure 26:** Filament arrangement within the reactor.

#### **4.5.2 Filament Heating**

The filament heat is generated through electrical resistance, the more power supplied the greater the heating. The temperature could not be measured directly *in situ* with a pyrometer due to the small filament area. Therefore, the operating power / temperature during growth runs was based on scaled up conditions from a smaller HF reactor in the lab. The smaller reactor supplies 250 W to  $3 \times 50$  mm, 0.25 mm diameter Ta filaments<sup>71</sup>. Scaling this to  $4 \times 70$  mm, 0.25 mm Ta filaments required a power of 466 W or 116 W per filament.

### 4.5.3 Filament Carburization

The presence of carbon feedstock and extreme temperatures mean the filaments carburize during growth runs. This can be advantageous as the melting point of Ta carbide is much hotter than Ta, allowing higher temperatures to be reached, increasing growth rates<sup>28</sup>. However, carburization weakens the filaments and limits their operational life-time to 8 h. In addition, as the filaments carburize they act as a carbon sink reducing carbon available for diamond growth, reducing growth rates until complete carburization. To mitigate against this, growth runs with new filaments were run for 4 h instead of 3 h.

### 4.6 Reactor Operation

Seeded samples were loaded and secured in place by stainless steel clamps, with a filament-substrate distance of 4 mm. The reactor was pumped down to vacuum (0.2 Torr). CH<sub>4</sub> and H<sub>2</sub> (at rates of 2/200 sccm, respectively) were admitted into the reactor for 15 minutes and the pressure brought up to 20 Torr. The separate water chiller unit (UNIT NAME) was then turned on allowing water to flow in and out of the walls of the reactor. The reactor heater was then powered, and the filament power slowly dialled up to 116 W per filament (3 filaments = 350 W, 4 filaments = 466 W). The filament brightness was checked through the viewing window to ensure all wires had current passing through them, i.e. they were glowing white hot (Figure 27).

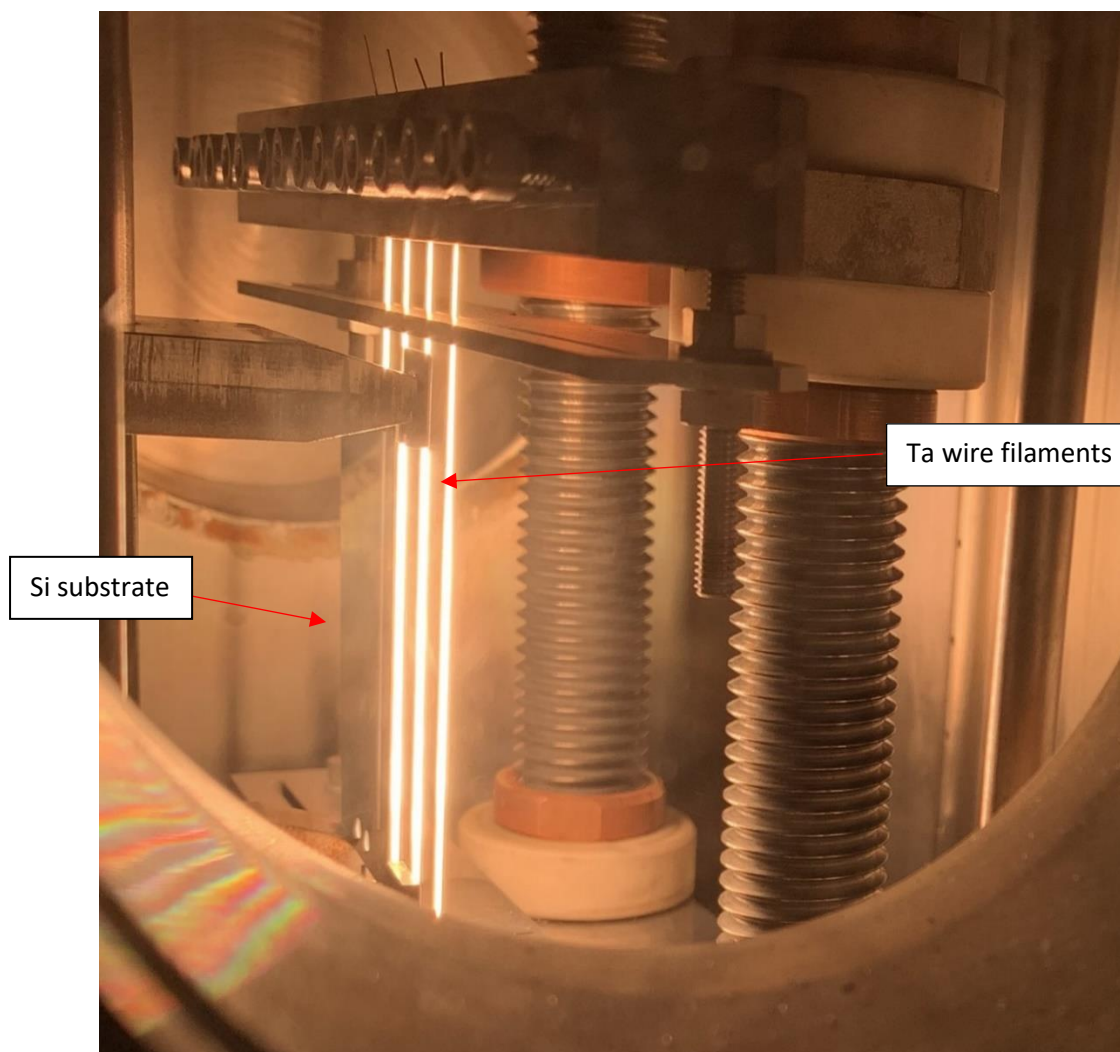


**Figure 27:** View from side window of the reactor during operation.

#### **4.7 Shutting down**

The reactor shutdown procedure was identical for all runs. The methane flow was stopped and hydrogen flow was continued for 5 minutes with the filaments still powered. This was to clean up any residual graphitic carbon on the diamond film surface. The filament power was then reduced to zero slowly over a period of about 1 min, and the hydrogen flow was stopped. The reactor was then pumped down to vacuum (0.2 Torr). After 30 minutes the water cooling was shut off and the chamber brought up to atmospheric pressure (approx. 760 Torr) and the samples were removed. Vibrations from opening of the reactor lid caused movement of the filament weights, frequently breaking the brittle carburized filaments before their 8 h life-time had elapsed.

#### **4.8 Experiments**

Two series of experiments were carried out. The first set (labelled TSX, where X indicates sample number) were used to commission the reactor and show viable seeded methodology. The second set (labelled ISX, where X indicates sample number) were the ISIS samples grown at varying conditions.

Table 2: Outline of samples and their growth conditions.

<b>Sample</b>	<b>Seeding <sup>a</sup></b>	<b>New Filaments <sup>b</sup></b>	<b>Num. Filaments</b>	<b>Growth time / h<sup>-1</sup></b>	<b>CH<sub>4</sub> Conc. / %</b>
TS1	S	Yes	3	1	1
TS2	S	No	3	3	1
TS3	S	No	3	3	1
TS4	S	Yes	4	3	1
TS5	S	Yes	4	3	1
IS1	S	Yes	4	4	1
IS2	S	Yes	4	3	1.5
IS3	D	Yes	4	4	1
IS4	D	No	4	3	1.5
IS5 <sup>c</sup>	D	Yes	4	6.5	1

<sup>a</sup> S = single seeding, D = double seeding. <sup>b</sup> Filament replacement was inconsistent. Filaments were either replaced before their 8 h lifetime or after breaking due to their fragility. <sup>c</sup> The growth of sample IS5 was not part of the main project and is discussed in Appendix 1.

## **5. Commissioning of the Large Area HF CVD Reactor**

### **5.0 Raman Characterisation**

Raman spectroscopy provides a rapid and non-destructive method to characterise diamonds purity and crystallinity. The Raman spectrometer used was a Renishaw 2000, with a 514 nm laser, calibrated before each spectrum with single crystal diamond. The purity of diamond is assessed by the intensity of its Raman peak (at  $1332.6\text{ cm}^{-1}$ ) in relation to that of  $\text{sp}^2$  graphite peaks (at  $1370$  and  $1580\text{ cm}^{-1}$ ).

Diamond's characteristic peak at  $1332.6\text{ cm}^{-1}$  corresponds to excitation in its  $\text{T}_{2g}$  vibrational mode<sup>72</sup>. The graphite peak at  $1580\text{ cm}^{-1}$  corresponds to excitation in the  $\text{E}_{2g}$  vibrational mode of the ordered graphite rings, this is denoted the G-band<sup>73</sup>. The graphite peak at  $1370\text{ cm}^{-1}$  corresponds to excitation in disordered graphite, and is denoted the D-band<sup>74</sup>. The use of a visible light laser means the  $\pi$  states of graphite are disproportionally excited and graphite peaks appear much larger ( $\sim 50\times$ ) than their concentration in relation to the diamond peak<sup>75, 76</sup>.

The crystallinity of the diamond was assessed by measuring the full-width half-maximum (FWHM) of the diamond peak which was compared to typical literature values for polycrystalline diamond  $\sim$  approximately  $6 - 18\text{ cm}^{-1}$ <sup>72</sup>.

## 5.1 Results



**Figure 28:** Raman spectrum from samples TS2 (blue) and TS3 (red) – diamond grown on a Si substrate. Single nano-diamond seeded sample, growth conditions 1 % CH<sub>4</sub> for 3 h, with 3 × 7.25 cm Ta filaments, 350 W. The diamond peaks for TS2 and TS3 were recorded at 1332 cm<sup>-1</sup>.

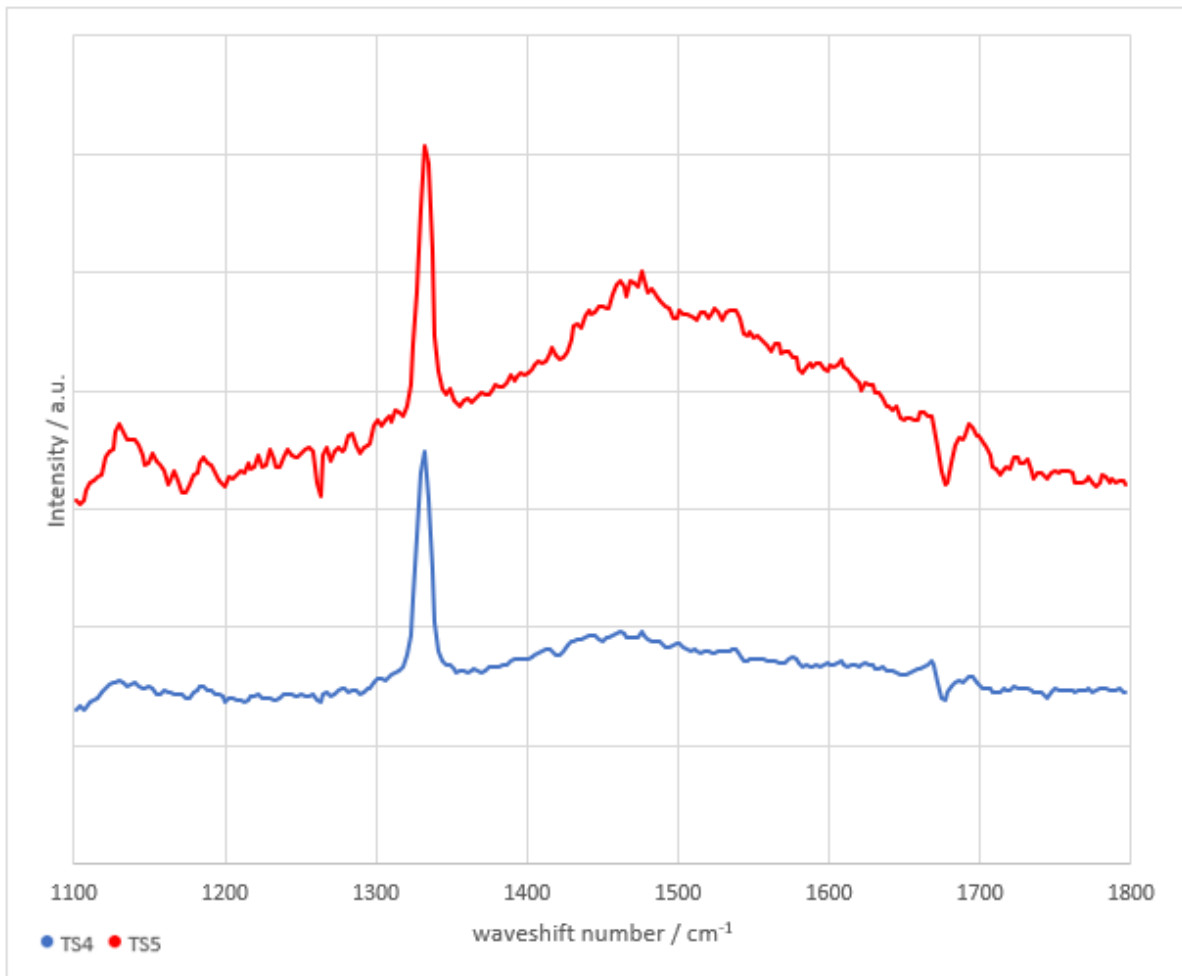


**Figure 29:** Raman spectrum for samples TS4 (blue) and TS5 (red) - diamond grown on a Si substrate. Single nano-diamond seeded, growth conditions 1 % CH<sub>4</sub> for 3 h, with 4 × 7 cm Ta filaments, 466 W. TS4 provided the least graphitic test sample. The diamond peaks were recorded at 1332 cm<sup>-1</sup> and 1334 cm<sup>-1</sup> respectively.

## 5.2 Discussion

The reactor was tested with diamond growth of five Si samples (TS1-5). The initial growth run (TS1) tested the functionality of the reactor components (stability of power, pressure and gas flow rate) and was not subjected to characterisation. The growth run also served to carburize the filaments. The sample was grown using  $3 \times$  Ta filaments for 1 h at 300 W power and 1 %  $\text{CH}_4$ . Throughout the growth run the power, pressure and gas flow rate remained consistent with no observable deviation. The reactor was deemed operational for sample growth runs.

### 5.2.1 Samples TS2-3

Diamond films were grown on samples TS2-3 (**Figure 30**) using  $3 \times$  carburised Ta filaments for 3 h at 350 W power and 1 %  $\text{CH}_4$ . The filament arrangement was such that the central filament aligned with the centre of the sample with a filament spaced either side at a distance of 10 mm.

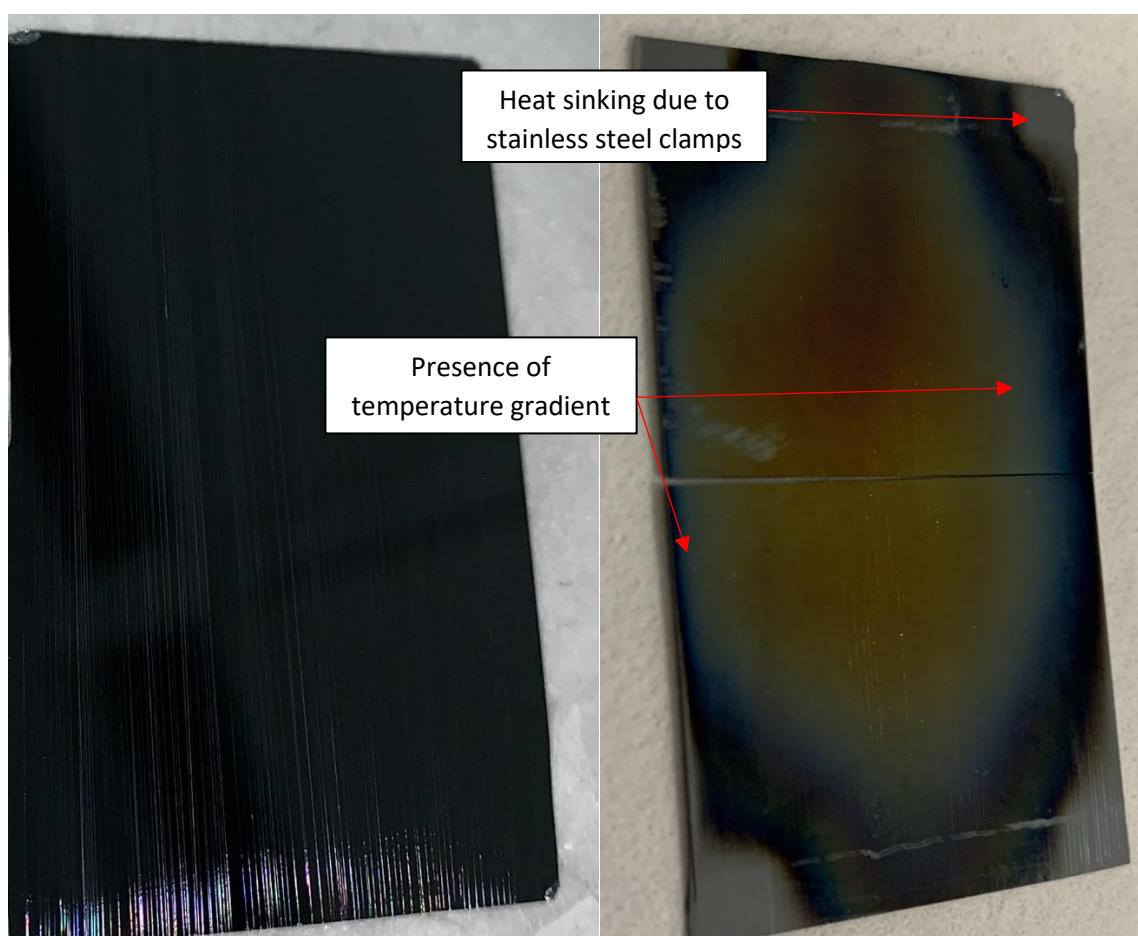


**Figure 30:** Photograph of sample TS3 ( $30 \times 50$  mm Si plate, scored vertically and seeded with nano-diamond) (Left) before growth and (Right) after the growth for 3 h at 350 W power. The sample sheared horizontally during growth along a pre-existing defect. No other samples exhibited structural failure during growth.

Both films exhibited a visible growth gradient across the sample (**Figure 30**). The central area covered by all three filaments has a uniform coating, however, toward the outside edge' diamond growth is visibly decreased. The cause is likely due to the distance from the filament, previous work has reported diminished diamond growth in regions  $\sim 5$  mm outside of filament coverage<sup>71</sup>. The black area is likely due to increased graphite growth in the lower-temperature area.

The corners of the sample exhibit no visible growth and diminished growth in the surrounding region. This is likely due to the holding clamps (**Figure 25**) blocking the surface from the filament heat and acting as a heat sink to the surrounding area. This feature was present in all samples.

The Raman spectra (**Figure 28**) were taken in the centre of the uniform growth region to analyse the purity of deposited films. The films (**Figure 28**) each show a strong diamond peak at  $1332\text{ cm}^{-1}$ . The average FWHM of the Raman diamond peaks was  $12.46\text{ cm}^{-1}$  which is within the normal range of crystallinity for poly crystalline diamond. Both samples exhibited a broad graphite peak around  $1500\text{ cm}^{-1}$  due to the presence of ordered graphite (G-band).

### 5.2.2 Samples TS4-5

Diamond films were grown on samples TS4-5 (**Figure 31**) using  $4 \times$  Ta filaments for 3 h at 466 W power and 1 %  $\text{CH}_4$ . The filament arrangement was such that both outside edges aligned with a filament with the other two filaments between them, each with a spacing of 10 mm.

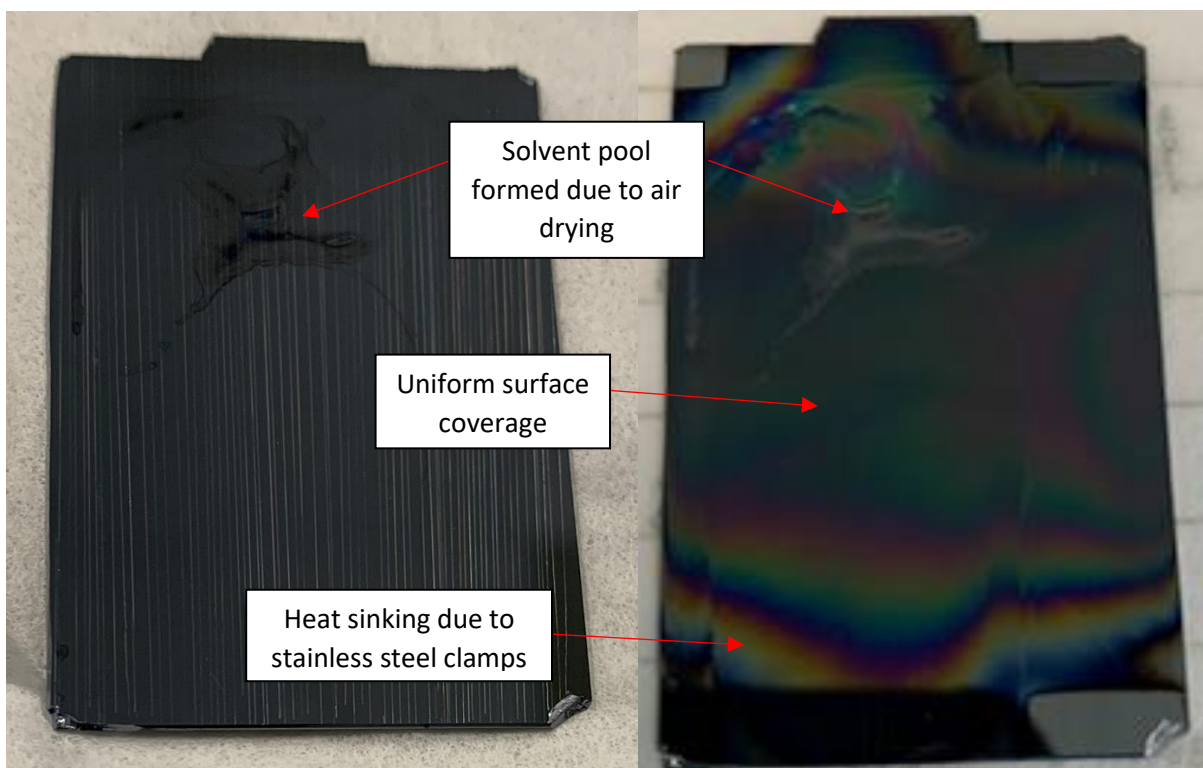


**Figure 31:** Photograph of sample TS4 ( $30 \times 50\text{ mm}$  Si plate, scored vertically and seeded with nano-diamond) (Left) before growth and (Right) after the growth of 3 h at 466 W power.

Both samples TS4 and TS5 had uniform central coverage (**Figure 31**) and the growth gradient across the central portion of the sample, observed in samples TS2-3, was not present. It is believed the increased filament coverage created a more uniform surface temperature across the sample, giving more uniform growth.

During the air drying of sample TS4 a solvent pool formed on the surface which caused distortion to the diamond film growth (**Figure 31**). Subsequently all further samples were dried using a compressed air gun to prevent solvent pools forming.

The Raman spectra (**Figure 29**) were taken in the same region as samples TS2-3. Sample TS4 shows a strong diamond peak at  $1332\text{ cm}^{-1}$ . Sample TS5 also shows a similarly strong diamond peak which is slightly shifted at  $1334\text{ cm}^{-1}$ . The FWHM of the samples were  $11.87\text{ cm}^{-1}$  and  $13.06\text{ cm}^{-1}$ ,

respectively, which is comparable to the crystallinity of samples TS2-3. Sample TS5 showed an increased graphite band compared with the other samples. The growth conditions were identical to the growth of sample TS4, so the origin of the increased graphitisation is unclear. It is possible that the use of non-carburised filaments with a growth time of 3 h did not allow sufficient time for sample deposition and graphite etching, leading to the increased graphite presence. However, the Raman used was a visible light (514 nm) laser which resonantly enhanced the  $\pi$  states of the graphite<sup>75,76</sup>. This means small increases in graphitisation result in a considerable enhancement to the graphite peak (72  $\times$  larger), but the film remains of high purity. The increased graphitisation was therefore not considered an issue.

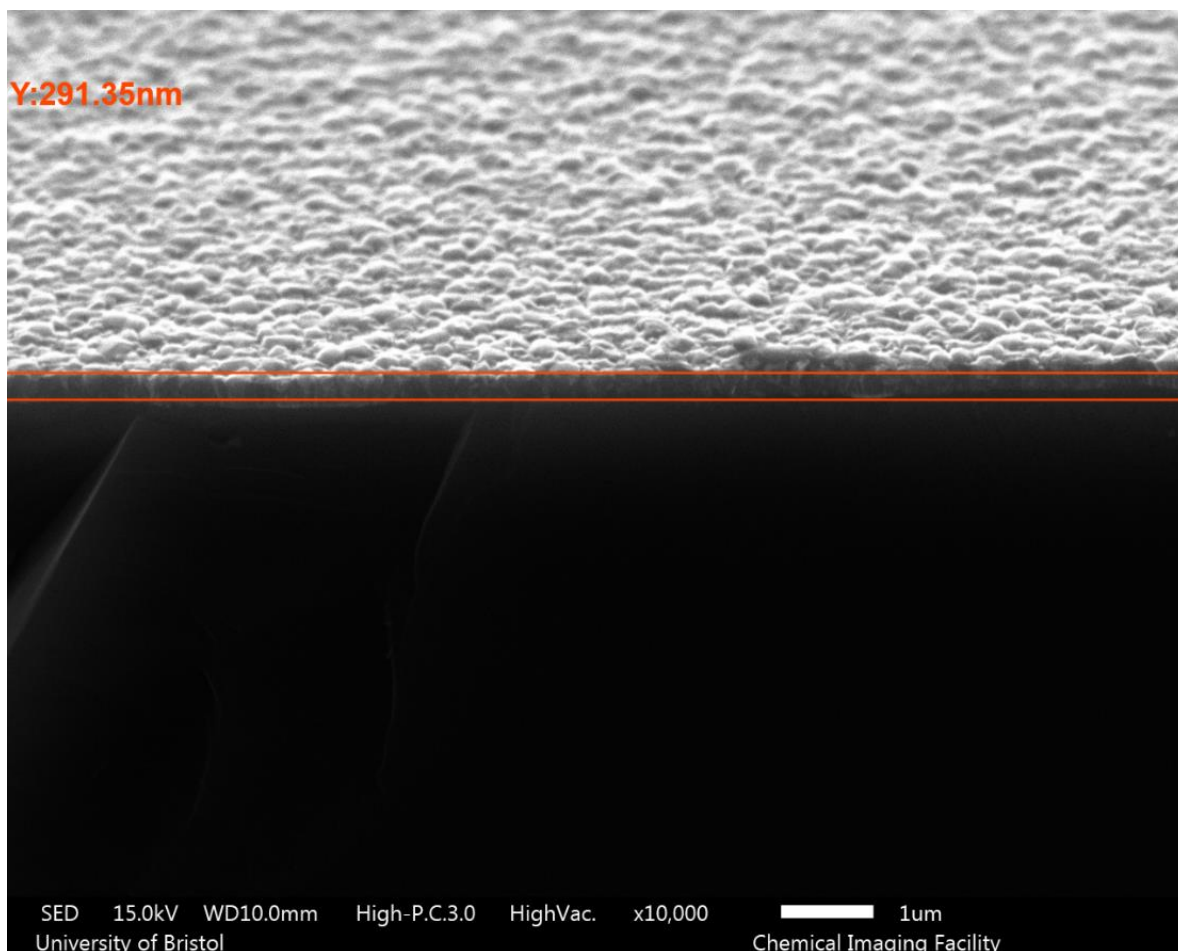


**Figure 32:** SEM image taken from the centre of TS4, diamond grown on Si at 1% CH<sub>4</sub>, 3 h at 466 W power. Two parallel orange lines along the Y-axis show the average film thickness of 291.35 nm. The SEM image was taken by Dr Jean-Charles Eloi of the University of Bristol's Chemical Imaging Facility.

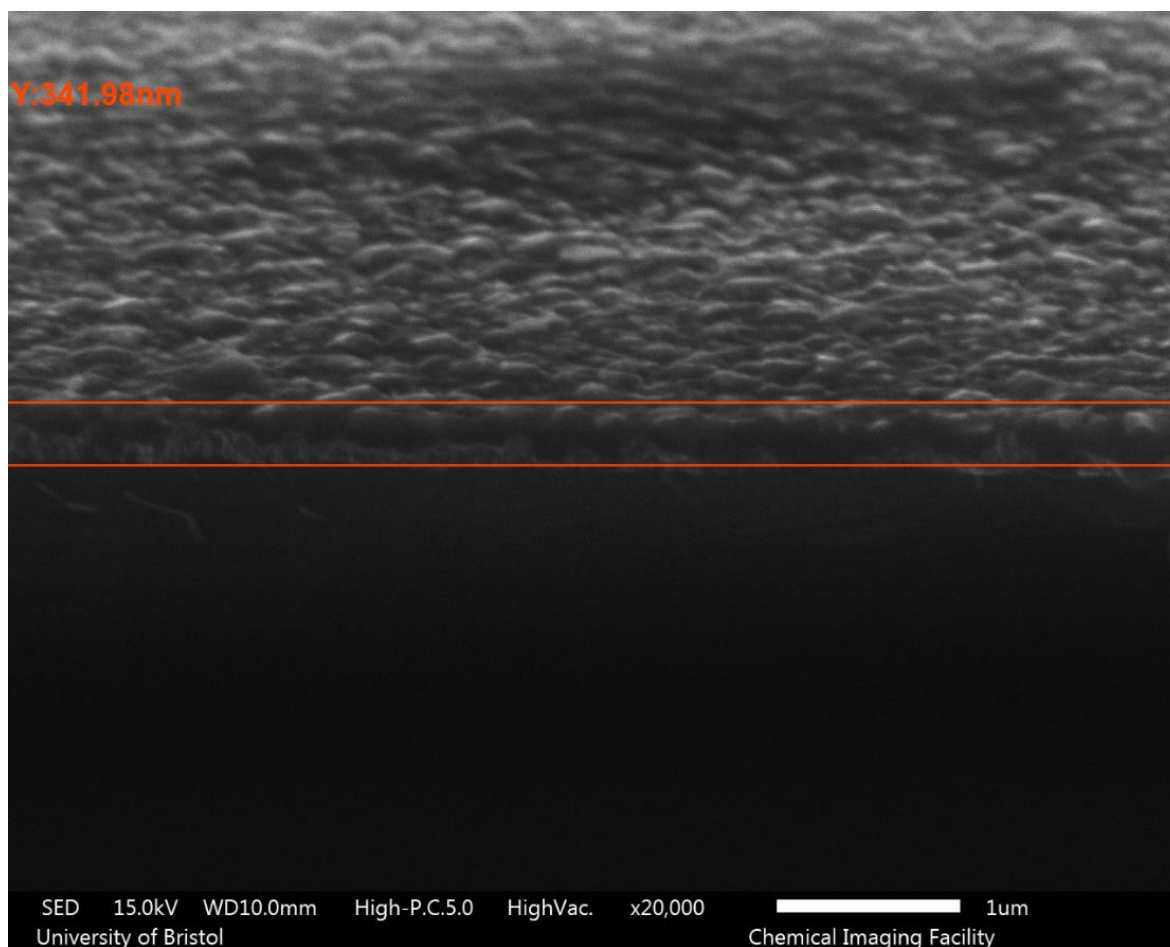


**Figure 33:** SEM image taken from the centre of TS5, diamond grown on Si at 1% CH<sub>4</sub>, 3 h at 466 W power. Two parallel orange lines along the Y-axis show the average film thickness of 341.98 nm. The SEM image was taken by Dr Jean-Charles Eloi of the University of Bristol's Chemical Imaging Facility.

Samples TS4-5 were imaged by to SEM (**Figures 32 & 33**) to provide information about film thickness and grain size. The images were taken near the centre of the films. The average film thickness after the 3 h growth was approximately 316 nm. The growth rate was approximately 100 nm h<sup>-1</sup>, which was far lower than the expected 300 - 500 nm h<sup>-1</sup>. However, both samples were grown using uncarbonized filaments which could have initially acted as a carbon sink, lowering the growth rate. This would mean a lower initial growth rate, but would then increase with time. The grain size was smaller than expected, on the order of a few hundred nm. Similarly to thickness, this was likely due to the lower initial growth and which did not allow the crystals to grow to the expected grain size (~1 µm). To increase film thickness future growth runs using uncarbonized filaments should be grown for a longer period of time.

## 6. Growth of ISIS Electron Stripping Films

### 6.1 Results

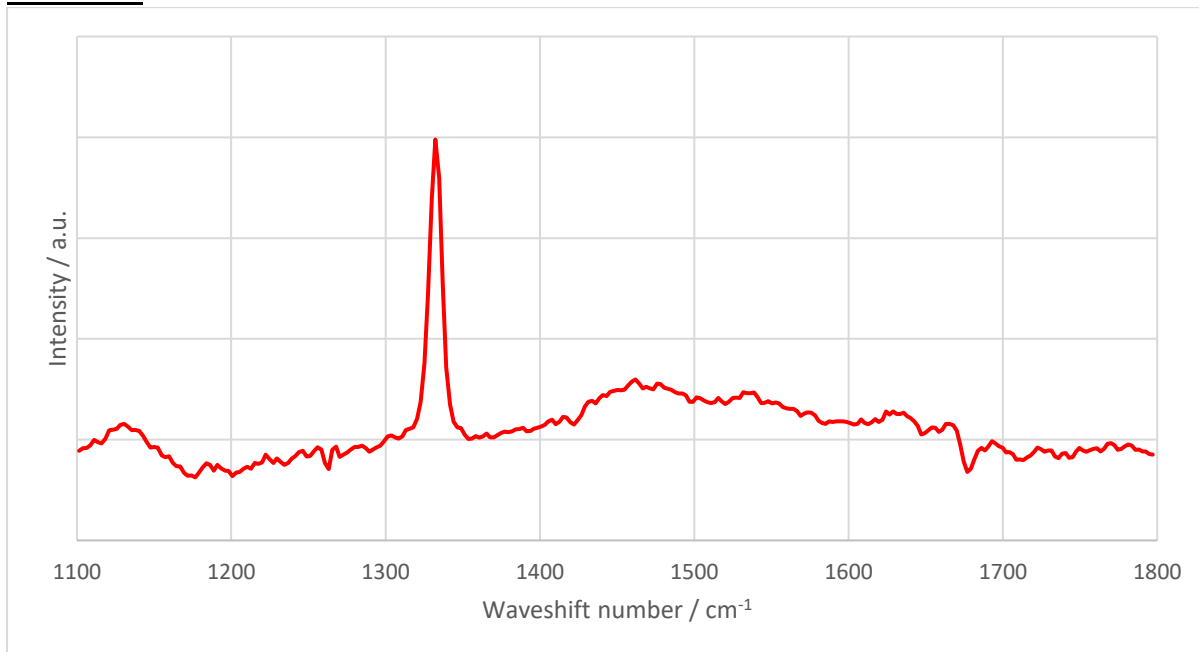


**Figure 34:** Raman spectrum of sample IS1 – diamond grown on a Si substrate. Single nano-diamond seeded sample, growth conditions 1 % CH<sub>4</sub> for 4 h. This provided the most crystalline and least graphitic diamond growth out of the ISIS sample runs. The diamond peak was recorded at 1333.8 cm<sup>-1</sup> and had a FWHM of 6.86 cm<sup>-1</sup>.

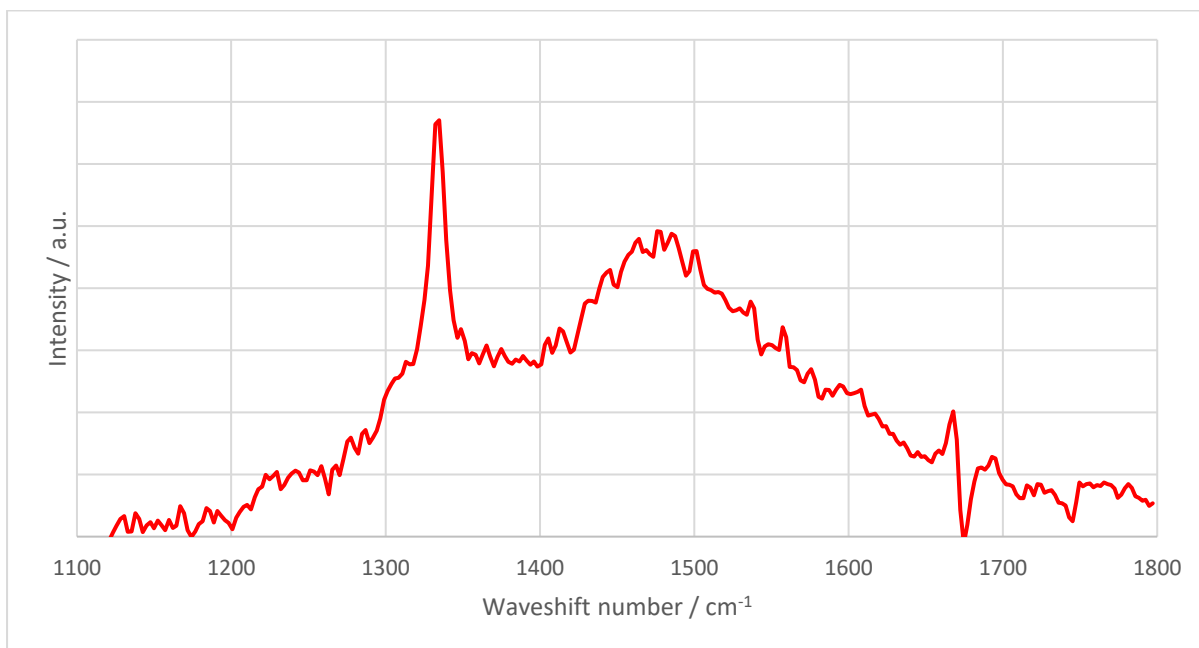


**Figure 35:** Raman spectrum of sample IS2 – diamond grown on a Si substrate. Single nano-diamond seeded sample, growth conditions 1.5% CH<sub>4</sub> for 3 h. This resulted in the most graphitic diamond growth of the single seeded samples. The diamond peak was recorded at 1334.2 cm<sup>-1</sup> and had a FWHM of 10.64 cm<sup>-1</sup>.

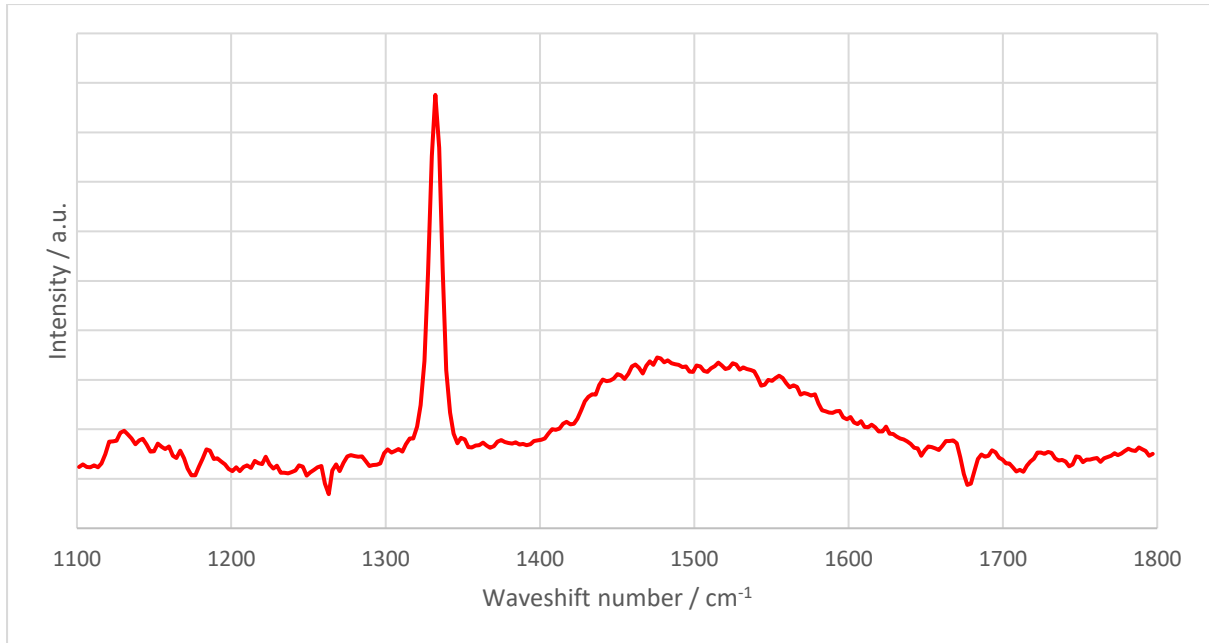


**Figure 36:** Raman spectrum of sample IS3 – diamond grown on a Si substrate. Double nano-diamond seeded sample, growth conditions 1 % CH<sub>4</sub> for 4 h. This resulted in the most crystalline and least graphitic of the double seeded samples. The diamond peak was recorded at 1332.3 cm<sup>-1</sup> and had a FWHM of 9.07 cm<sup>-1</sup>.

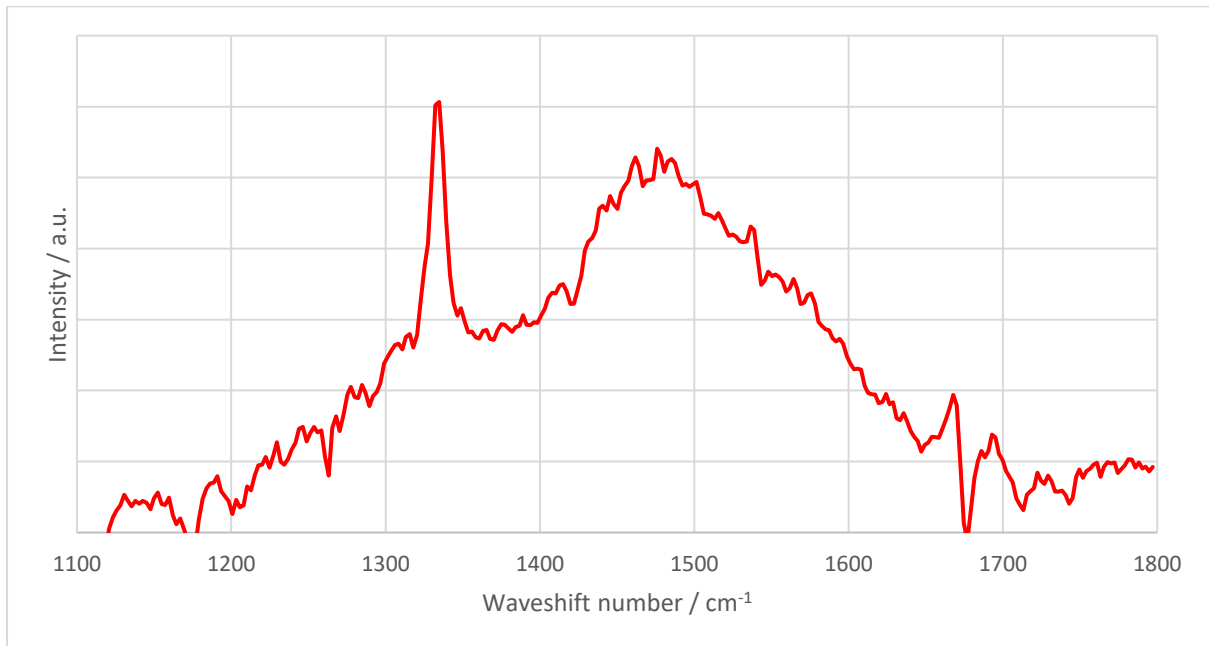


**Figure 37:** Raman spectrum of sample IS4 – diamond grown on a Si substrate. Double nano-diamond seeded, growth conditions 1.5 % CH<sub>4</sub> for 3 h. This resulted in the most graphitic of the double seeded samples. The diamond peak was recorded at 1334.6 cm<sup>-1</sup> and had a FWHM of 11.08 cm<sup>-1</sup>.

## 6.2 Discussion

The work outlined in section 5 established the growth parameters for a uniform diamond coating on the samples. The growth of samples IS1-4 then saw variations to the process (outlined in **Table 2**) to reduce the presence of pin-holes whilst maintaining a high quality of diamond film.

Diamond films were grown on four Si plates (an example of which is shown by **Figure 38**) for the ISIS Neutron and Muon source. The  $30 \times 55$  mm films will be supported along one edge, *via* the two mounting holes, in the ISIS synchrotron (as discussed in **Section 3.5**). The patterned surface provides mechanical support to the film preventing the failures exhibited by other carbon based films<sup>66</sup>. Maintaining a uniform diamond coating across the sample was imperative so that the pattern was incorporated.

### 6.2.1 IS1

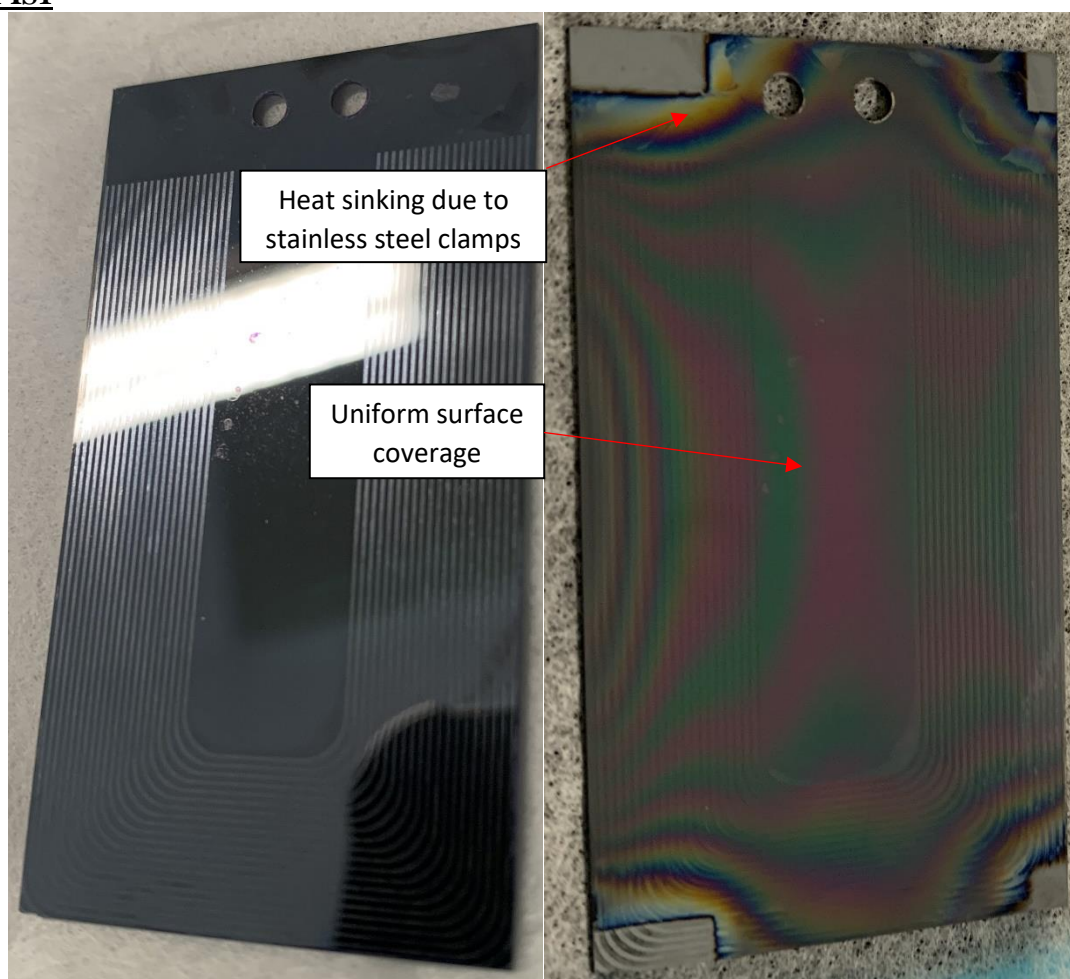


**Figure 38:** Photograph of sample IS1 ( $30 \times 55$  mm Si plate, patterned by the ISIS Neutron and Muon source and seeded with nanodiamond) (Left) before and (Right) after growth for 4 h with uncarbonized Ta filaments at 466 W power.

Sample IS1 was single seeded and grown for 4 h at 1 %  $\text{CH}_4$  and 466 W power. The sample had a uniform diamond coating (**Figure 38**) across the middle section. Under an optical microscope ( $50 \times$  magnification) some pin-holes were visible in the sample film. These were however at a reduced rate compared to sample TS2-5. Due to time constraints, the number of pin-holes for samples IS1-4 were not quantified by SEM. Future work should include SEM of the film surfaces to quantify the number of pin-holes. This would then allow for numerical comparison between the growth conditions and pin-hole number.

Similarly to samples TS2-5, the corners exhibited a temperature gradient due to the sample clamp. However, the growth gradient in IS1 was less pronounced. It is believed the additional heating time raised the clamp temperature, reducing heat sinking and producing a more uniform sample. The clamps also blocked the corners of the sample from any diamond growth. This may result in reduced mechanical strength as the pattern is incomplete. It is suggested for future work a larger Si plate be used with a waste section at the base so the pattern can be completely covered.

The Raman spectrum (see **Figure 34**) showed a slightly shifted diamond peak at  $1333.8\text{ cm}^{-1}$ . The FWHM of the peak was  $6.86\text{ cm}^{-1}$ , which is highly crystalline for a polycrystalline diamond film and was the most crystalline of all the ISIS samples. The Raman also showed IS1 to be the purest and least graphitic of the samples. It is thought the longer growth time and lower  $\text{CH}_4$  concentration, compared with samples IS2-4, allowed for less graphite formation and greater etching producing a more pure and crystalline sample.

### **6.2.2 IS2**

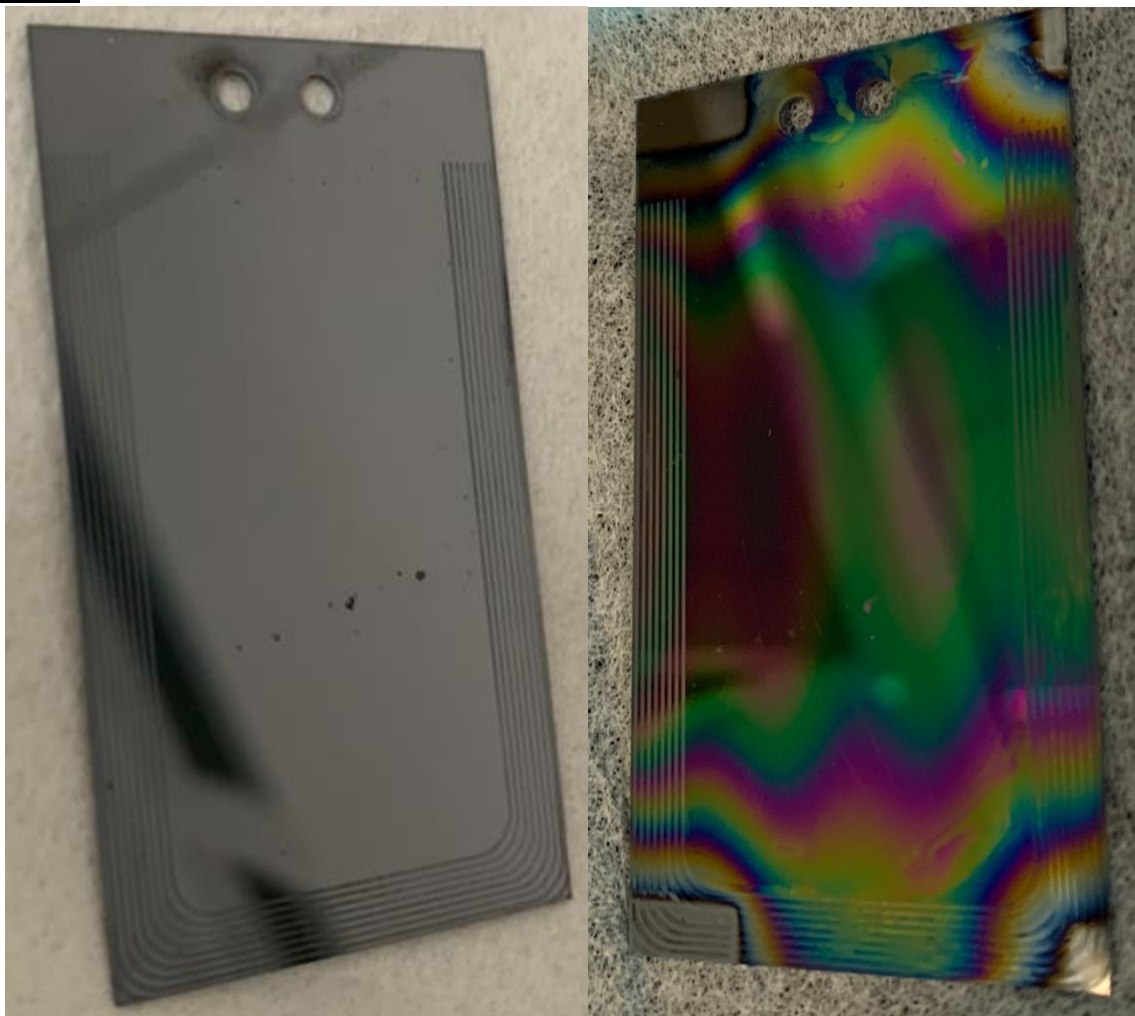


**Figure 39:** Photograph of sample IS2 ( $30 \times 55\text{ mm}$  Si plate, patterned by the ISIS Neutron and Muon source and seeded with nanodiamond) (Left) before and (Right) after growth for 3 h with uncarbonized Ta filaments at 466 W power in 1.5%  $\text{CH}_4$ .

Sample IS2 (see **Figure 39**) was single seeded and grown for 3 h at 1.5 %  $\text{CH}_4$  and 466 W power. The greater  $\text{CH}_4$  concentration was thought to increase diamond growth and reduce pin-hole number. The sample does not exhibit the same uniformity seen in samples TS4-5 and IS1. The film exhibits clear temperature gradients across the middle and around the clamp sites. It is believed the filaments were

bowed during mounting which initially created an uneven temperature distribution across the surface. The inconsistent heat could have then led to uneven initial diamond growth, and subsequent growth would have retained the uneven surface. The difference in film thickness across the surface is on the order of a few 10s of nm and insignificant compared to thickness of the overall film. Importantly, the sample maintained full-width coverage. As with all other samples, the corners also exhibited a temperature gradient due to the sample clamps. Under an optical microscope ( $50\times$  magnification) fewer pin-holes were visible in the sample compared to samples TS2-5 and IS1. This supports the idea that a greater  $\text{CH}_4$  concentration reduces the number of pin-holes, due to increased growth. However, as with sample IS1, this was not quantified.

The Raman spectrum (see **Figure 35**) showed a slightly shifted diamond peak at  $1334.2\text{ cm}^{-1}$ . The FWHM of the peak was  $10.64\text{ cm}^{-1}$ , which is less crystalline than sample IS1, however it is within the normal range for polycrystalline diamond. The Raman spectrum also showed IS2 to be more graphitic compared to IS1 with a graphite peak at  $1500\text{ cm}^{-1}$ . The sample is likely more graphitic due to the faster growth which would produce a more disordered sample. However, as referenced in section 5.0 the film remains of high purity as Raman is more sensitive to graphite<sup>75, 76</sup>.

### **6.2.3 IS3**

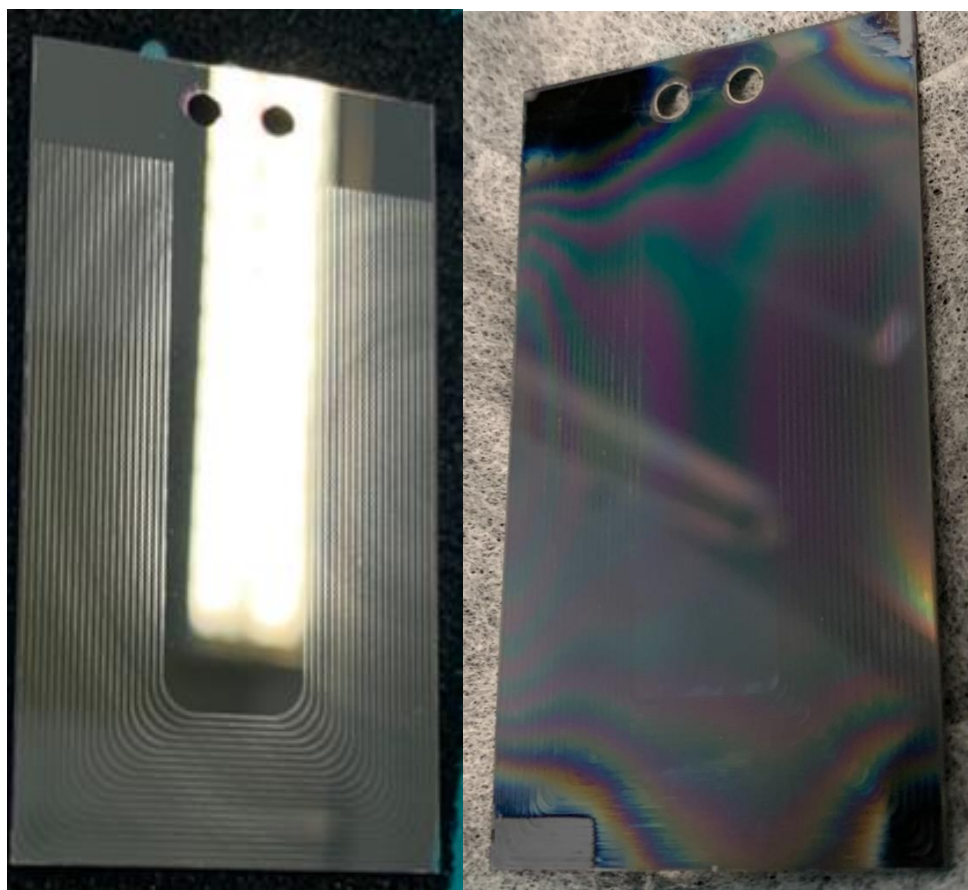


**Figure 40:** Photograph of sample IS3 ( $30\times 55\text{ mm}$  Si plate, patterned by the ISIS Neutron and Muon source and double seeded with nanodiamond) (Left) before and (Right) after growth for 4 h with uncarbonized Ta filaments at 466 W power in 1%  $\text{CH}_4$ .

Sample IS3 (see **Figure 40**) was double seeded and grown for 4 h at 1 %  $\text{CH}_4$  and 466 W power. It was hypothesised that double seeding would sufficiently increase the nucleation density to reduce the presence of pin-holes. The appearance and uniformity of the sample was comparable to IS1, grown under similar conditions. Under an optical microscope ( $50\times$  magnification) however, pin-hole presence was greatly reduced to that of samples IS1 and IS2. As with other samples this was not

quantified. As with all other samples, the corners exhibited a temperature gradient due to heat sinking *via* the sample clamp. Similarly with sample IS1, the growth gradient was less pronounced. This is similarly believed to be caused by the longer growth time which allowed the sample clamp to heat up, reducing heat sinking. As with samples IS1 and IS2, the corners were blocked from diamond growth which may compromise the mechanical strength implemented by the pattern.

The Raman spectrum (**Figure 36**) showed a strong diamond peak at  $1332.3\text{ cm}^{-1}$ . The FWHM of the peak was  $9.07\text{ cm}^{-1}$ , which is of comparable crystallinity to the other samples grown at 1 %  $\text{CH}_4$  and more crystalline than samples grown at 1.5 %  $\text{CH}_4$ . The results support the hypothesis that double seeding the sample reduces the pin-hole numbers without compromising the sample's crystallinity. The sample also showed a small graphite peak around  $1500\text{ cm}^{-1}$ .

#### **6.2.4 IS4**

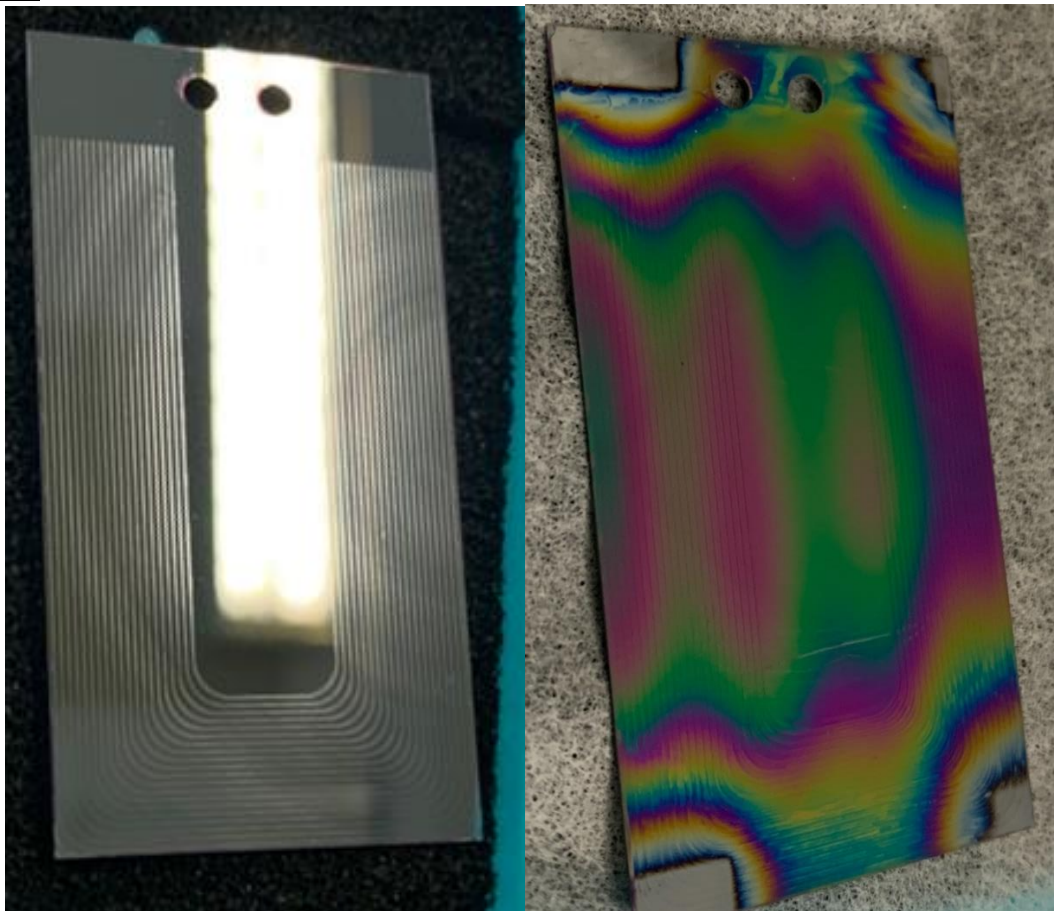


**Figure 41:** Photograph of sample IS2 ( $30 \times 55\text{ mm}$  Si plate, patterned by the ISIS Neutron and Muon source and seeded with nanodiamond) (Left) before and (Right) after growth for 3 h with carbonized Ta filaments at 466 W power in 1.5%  $\text{CH}_4$ .

Sample IS4 (see **Figure 41**) was double seeded and grown for 3 h at 1.5 %  $\text{CH}_4$  and 466 W power. In appearance, the sample was comparable with sample IS2 (see **Figure 39**). Both films exhibit a similar temperature gradient across the centre of the sample. It is believed that the higher  $\text{CH}_4$  concentration initiated growth more quickly, which did not allow enough time for the filaments to straighten under heating. Filaments that bowed toward the sample gave an uneven filament substrate distance, resulting in an uneven surface growth topography, which was retained during subsequent growth layers. However, as with sample IS2 the size difference is on the order of a few 10s of nm and is inconsequential in comparison to film thickness. Under an optical microscope ( $50 \times$  magnification)

sample IS4 had the fewest visible pin-holes compared to all other samples. However, as with other samples, this was not quantified. Future work should make use of further surface characterisation techniques, such as SEM, to quantify the number of pin-holes.

The Raman spectrum (**Figure 37**) showed a slightly shifted diamond peak at  $1334.6\text{ cm}^{-1}$ . The FWHM of the peak was  $11.08\text{ cm}^{-1}$ , which is comparable to that of IS2 however it is also the least crystalline of all ISIS samples. The crystallinity remains in the normal range for polycrystalline diamond. Similarly to IS2, the Raman for IS4 showed the sample to be more graphitic with a broad peak around  $1500\text{ cm}^{-1}$ . The increased graphitic presence is again believed to be caused by the increased  $\text{CH}_4$  concentration and faster growth it induces. Again, as referenced in section 5.0, the film is considered more graphitic in comparison to the other ISIS samples but is still high purity diamond as the Raman is more sensitive to graphite<sup>76</sup>.

## **7. Conclusions**

### **7.1 Summary**

The primary aim of this research was to commission the Bristol Diamond Groups large area CVD reactor. This was achieved and results have shown that the reactor can deposit diamond films over large areas ( $30 \times 55$  mm) provided the area is uniformly covered by hot filaments. Uniform coverage prevents a temperature gradient forming between the area directly below the filament and the areas 0.5 cm from the filament giving an even and higher quality film growth. From Raman data, it was shown the films were of high purity and of average crystallinity for polycrystalline films. With the reactor having capacity to cover  $15 \times 15$  cm wafers, the work indicates high quality diamond films can likely be grown over areas of this size.

The secondary aim was to grow diamond electron-stripping foils for the ISIS neutron and muon source, to the required specifications for use in their accelerator facility. The specifications were diamond films of micro- to nanometre grain size,  $1 \mu\text{m}$  thick and with no pinholes over an area of  $30 \times 55$  mm. Preliminary results indicate this aim has been achieved, however, further refinement and characterisation is required to ensure all specifications are met.

The surfaces of all samples exhibited growth of a uniform diamond layer across their smooth and patterned areas. Each corner had slight growth gradients and a blocked section caused by heat sinking and shielding due to the sample clamps. To prevent this future samples should include additional material on the bottom edge to be held by the clamps so as to ensure total sample coverage.

Raman data has shown all films exhibited a strong diamond signal with a high degree of purity. However, samples grown in 1.5%  $\text{CH}_4$  showed a greater graphite presence. Films grown at 1%  $\text{CH}_4$  were the most pure, and for future work the lower  $\text{CH}_4$  concentration is recommended. All samples exhibited crystallinity with-in the normal range for polycrystalline diamond coatings. The films grown for a longer period of time and with a lower  $\text{CH}_4$  concentration exhibited the most crystallinity. It is believed both factors contribute to increased etching of graphite giving a purer and more crystalline sample.

Film thickness was assessed *via* a combination of qualitative assessment and previous work's average growth rates. This was found to be approximately  $1\text{-}2 \mu\text{m}$  in thickness for a growth time of 3 h. Future work should include further characterisation, such as SEM, to quantify the growth rate in  $\mu\text{m h}^{-1}$ . Growth of exactly  $1 \mu\text{m}$  thickness would then simply be a case of adjusting the time.

Pin-hole numbers in the films were assessed qualitatively under an optical microscope, and it was found samples that were double seeded and grown for longer time period (4 h) exhibited fewer pin-holes. A combination of both of these factors is recommended for the most reduced pin-hole numbers whilst maintaining a higher sample purity and crystallinity. Future work should include further characterisation, such as SEM, to support this claim quantitatively.

This research is beneficial as a basis for establishing optimal growth conditions for diamond films over large areas, by assessing sample crystallinity, purity, uniformity and surface pinholes. Specifically, for the manufacture of diamond electron-stripping foils for use in the ISIS Neutron and Muon source's synchrotron, the sample seeding,  $\text{CH}_4$  concentration and growth time should be optimised so that samples have a high nucleation density and slower growth, producing more crystalline and un-perforated surfaces. Higher crystallinity would improve the mechanical strength of the film, allowing for longer lifetimes, whilst total surface coverage would prevent the H<sup>-</sup> beams passing through intact.

## **7.2 Future work**

The commissioning of the large area reactor opens the door for many areas of possible future work; the three key areas identified are: growth area, growth rates and grain size.

The reactor's large capacity would allow for diamond deposition on  $15 \times 15$  cm wafers, provided sufficient power is supplied to heat the wires. This is dependent on the functionality of the 10 kW, 210 A, 48 V power supply. Once operational, the reactor should then be capable of readily depositing high quality diamond films over the  $15 \times 15$  cm area.

It is known that the growth rate of HF CVD pales in comparison to that of the MW CVD. However, the economical scalability of HF CVD far exceeds that of MP CVD. It would therefore be advantageous to explore methods to increase the growth rate in the large-area reactor. Recently, growth of single-crystal diamond has been achieved at a rate of  $10 \mu\text{m h}^{-1}$  using carburized Ta filaments and a temperature of  $3000 \text{ }^\circ\text{C}$  on a SCD seed<sup>28</sup>. This would pose a 20 to  $30 \times$  increase than the current rate.

The grain size of deposited films can be adjusted *via* the gas ratios and introduction of Ar. Using a gas ratio of 90/10/1, Ar/H<sub>2</sub>/CH<sub>4</sub> ultrananocrystalline diamond (UNCD, grain size 5-7 nm) has been grown on SiO<sub>2</sub>/Si substrates<sup>32</sup>. The properties of UNCD are similar to SCD, which could be advantageous for future research.

In specific regards to the ISIS samples, future research should include SEM characterisation to quantitatively assess the presence of pin-holes and film thickness.

## 8. References

1. R. A. Khmel'nitskiy, *Physics-Uspekh*, 2015, **58**, 134-149.
2. J. E. Field, *Reports on Progress in Physics*, 2012, **75**, 126505.
3. Diamond Structure  
[https://wps.prenhall.com/wps/media/objects/439/449969/Media\\_Portfolio/ch13.html](https://wps.prenhall.com/wps/media/objects/439/449969/Media_Portfolio/ch13.html),  
(accessed 28 November 2022).
4. S. F. Mitura, *Journal of Achievements of Materials and Manufacturing Engineering*, 2006, **16**, 9-16.
5. J. Roeser, N. F. A. Alting, H. P. Permentier, A. P. Bruins and R. Bischoff, *Analytical Chemistry*, 2013, **85**, 6626-6632.
6. P. A. Nistor, P. W. May, F. Tamagnini, A. D. Randall and M. A. Caldwell, *Biomaterials*, 2015, **61**, 139-149.
7. C. Hebert, J. Warnking, A. Depaulis, L. A. Garcon, M. Mermoux, D. Eon, P. Mailley and F. Omnes, *Mater. Sci. Eng. C-Mater. Biol. Appl.*, 2015, **46**, 25-31.
8. P. W. May, M. Clegg, T. A. Silva, H. Zanin, O. Fatibello-Filho, V. Celorrio, D. J. Fermin, C. C. Welch, G. Hazell, L. Fisher, A. Nobbs and B. Su, *Journal of Materials Chemistry B*, 2016, **4**, 5737-5746.
9. K. Kanda, S. Yoshida, K. Yoneshima and H. Ando, *Diam. Films Technol.*, 1998, **8**, 93-103.
10. M. Labudovic and M. Burka, *IEEE Trans. Compon. Packaging Technol.*, 2003, **26**, 575-581.
11. D. Araujo, M. Suzuki, F. Lloret, G. Alba and P. Villar, *Materials*, 2021, **14**, 7081.
12. M. S. Gulley, P. B. Keating, H. C. Bryant, E. P. MacKerrow, W. A. Miller, D. C. Rislove, S. Cohen, J. B. Donahue, D. H. Fitzgerald, S. C. Frankle, D. J. Funk, R. L. Hutson, R. J. Macek, M. A. Plum, N. G. Stanciu, O. B. vanDyck, C. A. Wilkinson and C. W. Planner, *Physical Review A*, 1996, **53**, 3201-3210.
13. T. Stachel, *Physics-Condensed Matter*, 2009, **21**, 364206.
14. P. W. May, *Philosophical Transactions of the Royal Society of London. Series A: Mathematical, Physical and Engineering Sciences*, 2000, **358**, 473-495.
15. F. P. Bundy, H. T. Hall, H. M. Strong and R. H. Wentorfjun, *Nature*, 1955, **176**, 51-55.
16. J. C. Angus, H. A. Will and W. S. Stanko, *J. Appl. Phys.*, 1968, **39**, 2915-&.
17. H. Yamada, A. Chayahara and Y. Mokuno, *Diamond and Related Materials*, 2018, **87**, 143-148.
18. A. K. Mallik, S. Bysakh, K. S. Pal, N. Dandapat, B. K. Guha, S. Datta and D. Basu, *Transactions of the Indian Ceramic Society*, 2013, **72**, 225-232.
19. M. Schwander, *Diamond & Related Material*, 2011, **20**, 1287-1301.
20. B. V. Spitsyn, *Diamond and Related Materials* 1999, **8**, 1371-1376.
21. J. E. Butler, R. L. Woodin, L. M. Brown and P. Fallon, *Philosophical Transactions of the Royal Society of London. Series A: Physical and Engineering Sciences*, 1993, **342**, 209-224.
22. D. G. Goodwin, *Applied Physics Letters*, 1991, **59**, 277-279.
23. S. Yugo, T. Kanai, T. Kimura and T. Muto, *Applied Physics Letters*, 1991, **58**, 1036-1038.
24. M. Jiang, C. Chen, P. Wang, D. Guo, S. Han, X. Li, S. Lu and X. Hu, *Proceedings of the National Academy of Sciences*, 2022, **119**.
25. S. Ohmagari, H. Yamada, N. Tsubouchi, H. Umezawa, A. Chayahara, Y. Mokuno and D. Takeuchi, *Physica Status Solidi a-Applications and Materials Science*, 2019, **216**, 15.
26. Y. Takamori, M. Nagai, T. Tabakoya, Y. Nakamura, S. Yamasaki, C. E. Nebel, X. F. Zhang, T. Matsumoto, T. Inokuma and N. Tokuda, *Diamond and Related Materials*, 2021, **118**, 4.
27. P. Mason, PhD Thesis, University of Missouri, 2014.
28. T. Tabakoya, S. Kanada, Y. Wakui, Y. Takamori, T. Yamada, M. Nagai, Y. Kojima, O. Ariyada, S. Yamasaki, C. E. Nebel, T. Matsumoto, T. Inokuma and N. Tokuda, *Physica Status Solidi a-Applications and Materials Science*, 2019, **216**, 4.

29. J. J. Alcantar-Pena, E. de Obaldia, J. Montes-Gutierrez, K. Kang, M. J. Arellano-Jimenez, J. E. O. Aguilar, G. P. Suchy, D. Berman-Mendoza, R. Garcia, M. J. Yacaman and O. Auciello, *Diamond and Related Materials*, 2017, **78**, 1-11.
30. S. Ohmagari, H. Yamada, H. Umezawa, N. Tsubouchi, A. Chayahara and Y. Mokuno, *Diamond and Related Materials*, 2018, **81**, 33-37.
31. R. Haubner and B. Lux, *Diamond and Related Materials*, 1993, **2**, 1277-1294.
32. E. M. A. Fuentes-Fernandez, J. J. Alcantar-Peña, G. Lee, A. Boulom, H. Phan, B. Smith, T. Nguyen, S. Sahoo, F. Ruiz-Zepeda, M. J. Arellano-Jimenez, P. Gurman, C. A. Martinez-Perez, M. J. Yacaman, R. S. Katiyar and O. Auciello, *Thin Solid Films*, 2016, **603**, 62-68.
33. F. Silva, K. Hassouni, X. Bonnin and A. Gicquel, *J. Phys.-Condes. Matter*, 2009, **21**, 16.
34. D. King, M. K. Yaran, T. Schuelke, T. A. Grotjohn, D. K. Reinhard and J. Asmussen, *Diamond and Related Materials*, 2008, **17**, 520-524.
35. H. Yamada, A. Meier, F. Mazzocchi, S. Schreck and T. Scherer, *Diamond and Related Materials*, 2015, **58**, 1-4.
36. J. V. Silva Neto, J. S. Gómez, E. J. Corat and V. J. Trava-Airoldi, *Materials Research*, 2022, **25**.
37. J. Weng, F. Liu, L. W. Xiong, J. H. Wang and Q. Sun, *Vacuum*, 2018, **147**, 134-142.
38. J. Weng, J. H. Wang, S. Y. Dai, L. W. Xiong, W. D. Man and F. Liu, *Appl. Surf. Sci.*, 2013, **276**, 529-534.
39. H. Yamada, A. Chayahara, S. Ohmagari and Y. Mokuno, *Diamond and Related Materials*, 2016, **63**, 17-20.
40. W. X. Fei, M. Inaba, H. Hoshino, I. Tsuyusaki, S. Kawai, M. Iwataki and H. Kawarada, *Physica Status Solidi a-Applications and Materials Science*, 2019, **216**, 6.
41. NeoCoat CVDiam Reactors, (<https://www.neocoat.ch/en/products/cvdiam-equipments/hfcvd>, 2023).
42. O. Auciello and A. V. Sumant, *Diamond and Related Materials*, 2010, **19**, 699-718.
43. Q. Liang, C.-S. Yan, J. Lai, Y.-F. Meng, S. Krasnicki, H. Shu, H.-K. Mao and R. J. Hemley, *Crystal Growth & Design*, 2014, **14**, 3234-3238.
44. T. Teraji, M. Hamada, H. Wada, M. Yamamoto and T. Ito, *Diamond and Related Materials*, 2005, **14**, 1747-1752.
45. J. Weng, L. W. Xiong, J. H. Wang, S. Y. Dai, W. D. Man and F. Liu, *Diamond and Related Materials*, 2012, **30**, 15-19.
46. T. Tachibana, Y. Ando, A. Watanabe, Y. Nishibayashi, K. Kobashi, T. Hirao and K. Oura, *Diamond and Related Materials*, 2001, **10**, 1569-1572.
47. H. Mehedi, *Diamond & Related Material*, 2014, **47**, 58-65.
48. B. Baudrillart, *Diamond & Related Materials*, 2017, **75**, 44-51.
49. B. Baudrillart, F. Bénédic, A. S. Melouani, F. J. Oliveira, R. F. Silva and J. Achard, *physica status solidi (a)*, 2016, **213**, 2575-2581.
50. W. Becker, *International Journal of Oral and Maxillofacial Implants* 1994, **9**, 31-40.
51. B. Yashiro, M. Shoda, Y. Tomizawa, T. Manaka and N. Hagiwara, *Journal of Artificial Organs*, 2012, **15**, 244-249.
52. J. Zalieckas, P. Pobedinskas, M. M. Greve, K. Eikehaug, K. Haenen and B. Holst, *Diamond and Related Materials*, 2021, **116**, 6.
53. J. Kim, K. Tsugawa, M. Ishihara, Y. Koga and M. Hasegawa, *Plasma Sources Sci. Technol.*, 2010, **19**, 5.
54. A. Kromka, O. Babchenko, T. Izak, S. Potocky, M. Davydova, N. Neykova, H. Kozak, Z. Remes, K. Hruska, B. Rezek and T. Ltd, Brno, CZECH REPUBLIC, 2011.
55. M. Schreck, J. Asmussen, S. Shikata, J.-C. Arnault and N. Fujimori, *MRS Bulletin*, 2014, **39**, 504-510.
56. M. Muehle, M. F. Becker, T. Schuelke and J. Asmussen, *Diamond and Related Materials*, 2014, **42**, 8-14.
57. G. Janssen and L. J. Giling, *Diamond and Related Materials*, 1995, **4**, 1025-1031.

58. Y. Kato, H. Umezawa, S. Shikata and T. Teraji, *Diamond and Related Materials*, 2012, **23**, 109-111.
59. H. Yamada, A. Chayahara, H. Umezawa, N. Tsubouchi, Y. Mokuno and S. Shikata, *Diamond and Related Materials*, 2012, **24**, 29-33.
60. H. Yamada, A. Chayahara, Y. Mokuno, H. Umezawa, S. Shikata and N. Fujimori, *Appl. Phys. Express*, 2010, **3**, 3.
61. H. Yamada, A. Chayahara, Y. Mokuno, Y. Kato and S. Shikata, *Applied Physics Letters*, 2014, **104**, 102110.
62. H. Yamada, A. Chayahara, Y. Mokuno, N. Tsubouchi and S. Shikata, *Diamond and Related Materials*, 2013, **33**, 27-31.
63. ISIS Neutron and Muons Source <https://www.isis.stfc.ac.uk/Pages/About.aspx>, (accessed Feb, 2023).
64. About ISIS Neutron and Muon Source, <https://www.isis.stfc.ac.uk/Pages/About.aspx>, (accessed Feb, 2023).
65. How ISIS Works - in depth, <https://www.isis.stfc.ac.uk/Pages/How-ISIS-works--in-depth.aspx>, (accessed Feb, 2023).
66. B. Jones, *Initial Experience with Carbon Stripping Foils at ISIS*, IPAC, Busan Korea, 2016.
67. B. Jones, *An Overview of the Preparation and Characteristics of the ISIS Stripping Foil*, ISIS, STFC, Rutherford Appleton Laboratory, East-Lansing, MI, USA, 2014.
68. B. Jones, *Injection Upgrade on the ISIS Synchrotron*, ISIS, STFC, Rutherford Appleton Laboratory, Kyoto, Japan, 2010.
69. R. W. Shaw, V. A. Davis, R. N. Potter, L. L. Wilson, C. S. Feigerle, M. E. Peretich, C. J. Liaw and leee, *Corrugated thin diamond foils for SNSH(-) injection stripping*, IEEE, Knoxville, TN, 2005.
70. R. W. Shaw, A. D. Herr, C. S. Feigerle, R. I. Cutler, C. J. Liaw and Y. Y. Lee, *Thin diamond films for SNSH- injection stripping*, IEEE, Portland, OR, 2003.
71. E. Smith, PhD Thesis, University of Bristol, 2021.
72. K. Fabisiak, R. Torz-Piotrowska, E. Staryga, M. Szybowicz, K. Paprocki, A. Banaszak and P. Popielarski, *Mater. Sci. Eng. B-Adv. Funct. Solid-State Mater.*, 2012, **177**, 1352-1357.
73. R. Kostic, M. Miric, T. Radic, M. Radovic, R. Gajic and Z. V. Popovic, *Acta Phys. Pol. A*, 2009, **116**, 718-721.
74. S. Reich and C. Thomsen, *Philos. Trans. R. Soc. A-Math. Phys. Eng. Sci.*, 2004, **362**, 2271-2288.
75. M. A. Tamor and W. C. Vassell, *J. Appl. Phys.*, 1994, **76**, 3823-3830.
76. J. Filik, *Spectroscopy Europe*, 2005, **17**, 10-17.

## 9. Appendix 1: Sample IS5

The appendix covers the growth and SEM of sample IS5. The primary motivation for the growth run was to grow an ISIS sample plate ( **Figure A.1**) for an extended period of time and analyse it using SEM to assess the surface coverage. The increased growth-time meant the grain size and thickness were not representative of the other ISIS samples and thus are not discussed.

Sample IS5 (**Figure A.1**) was prepared and loaded using the same procedures as sample IS3 (explained in sections 4 and 6.2.3), however, the project timescale did not allow time for the growth run. The sample was later grown by James Smith and Paul May in the Bristol Diamond lab. The sample was grown for 6.5 h at 1% CH<sub>4</sub> at 466 W power using 4 × 7 cm uncarbonized Ta filaments. The sample was then characterised *via* SEM by Jean-Charles Eloi of the University of Bristol's Chemical Imaging Facility.

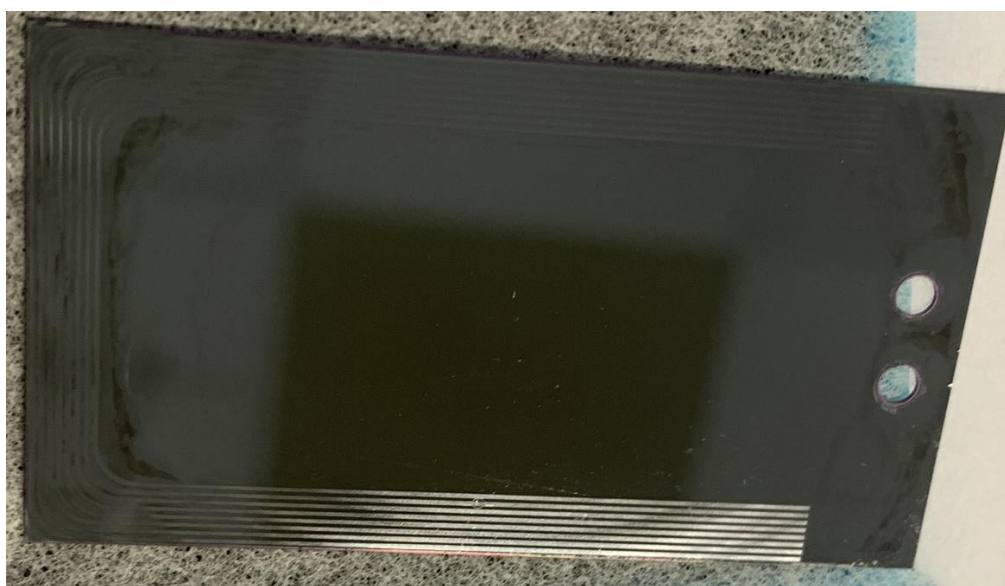


**Figure A.1:** Photograph of sample IS2 (30 × 55 mm Si plate, patterned by the ISIS Neutron and Muon source and seeded with nanodiamond) before growth.

The SEM images of the central portion of sample IS5 (**Figure A.2**) show good uniformity and no pin-hole presence. Consistent with samples IS3-4, this supports the hypothesis that double seeding the samples with nano-diamond reduces the pin-hole presence. The SEM images of the linear portion of the patterned section of IS5 (**Figures A.3, A.4 and A.5**) show total surface coverage of the pattern and no pin-hole presence. There is a uniform even coating across the sample moving outwards. No region was beyond a 5 mm radius from a filament. It is thought the even surface heating and seeding allowed for uniform growth across the entire surface. The SEM images of the curved portion of the patterned section of IS5 (**Figure A.6**) also show complete surface coverage. Particularly of note is the uniform and even coating up the side walls of the pattern (**Figure A.6.1-2**). This supports the use of dip seeding to uniformly coat a 3D surface evenly.

However, IS5 was grown for far longer than samples IS1-4 and therefore is indicative but not representative of their surface morphology. As discussed in section 7, future work should include SEM of samples grown under the same conditions. This would provide a more accurate insight and allow for conclusion about film thickness, grain size and presence pin-hole.

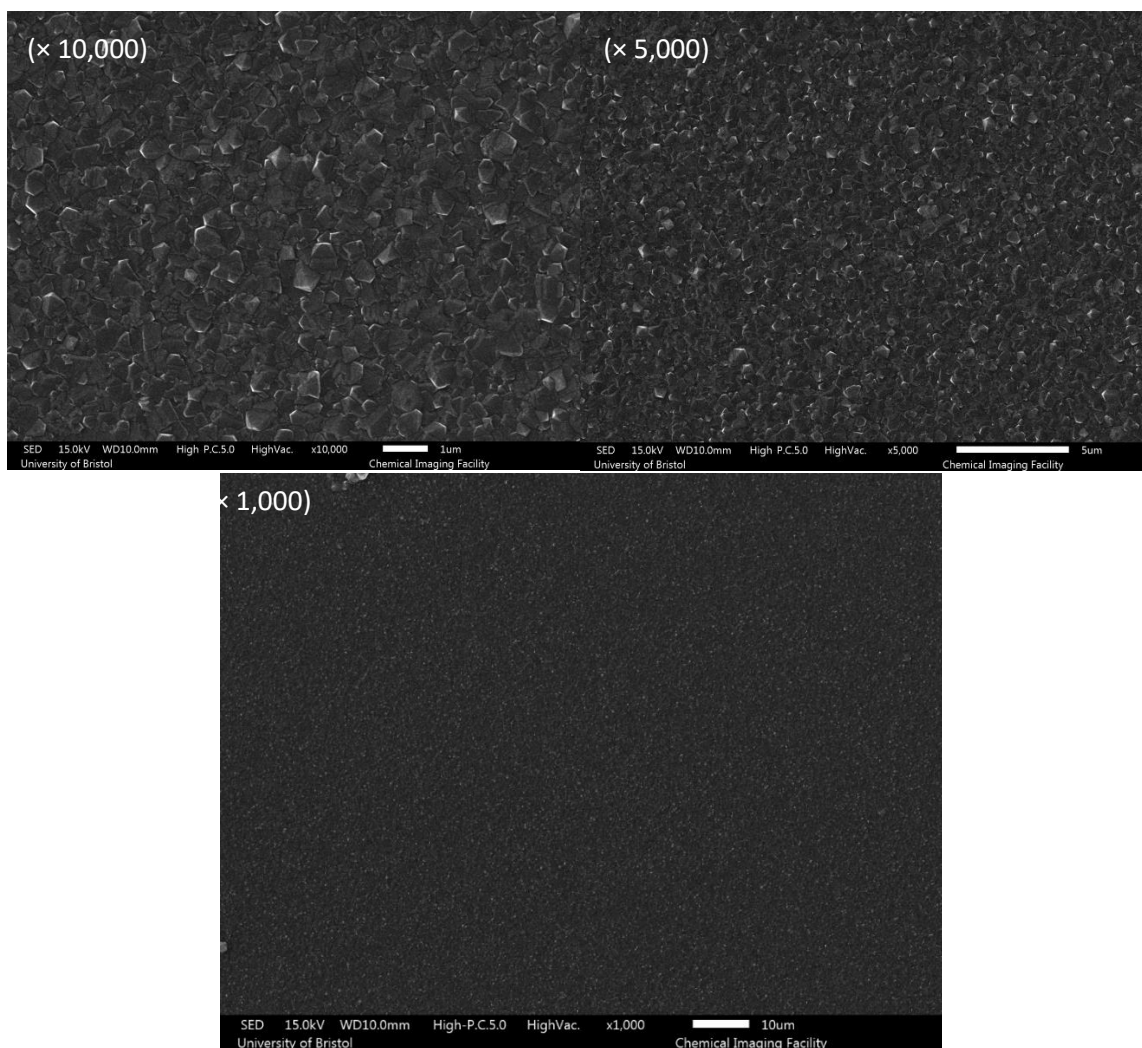


**Figure A.2:** SEM image of the middle of IS5 at  $\times 10,000$ ,  $\times 5,000$  and  $\times 1,000$  magnification. The SEM images were taken by Dr Jean-Charles Eloi of the University of Bristol's Chemical Imaging Facility.

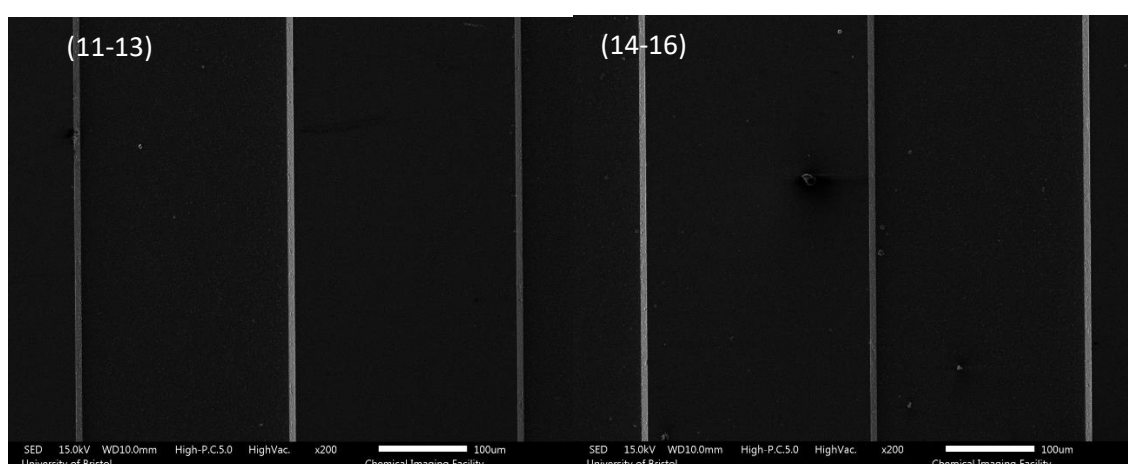


**Figure A.3:** SEM image of the left-side pattern lines of sample IS5. Diamond grown on Si plate for 6.5 h. Image 11-13 are the 11-13<sup>th</sup> lines from centre, image 14-16 are the 14-16<sup>th</sup> lines from the centre. The images were taken at  $\times 200$  magnification. The SEM images were taken by Dr Jean-Charles Eloi of the University of Bristol's Chemical Imaging Facility.

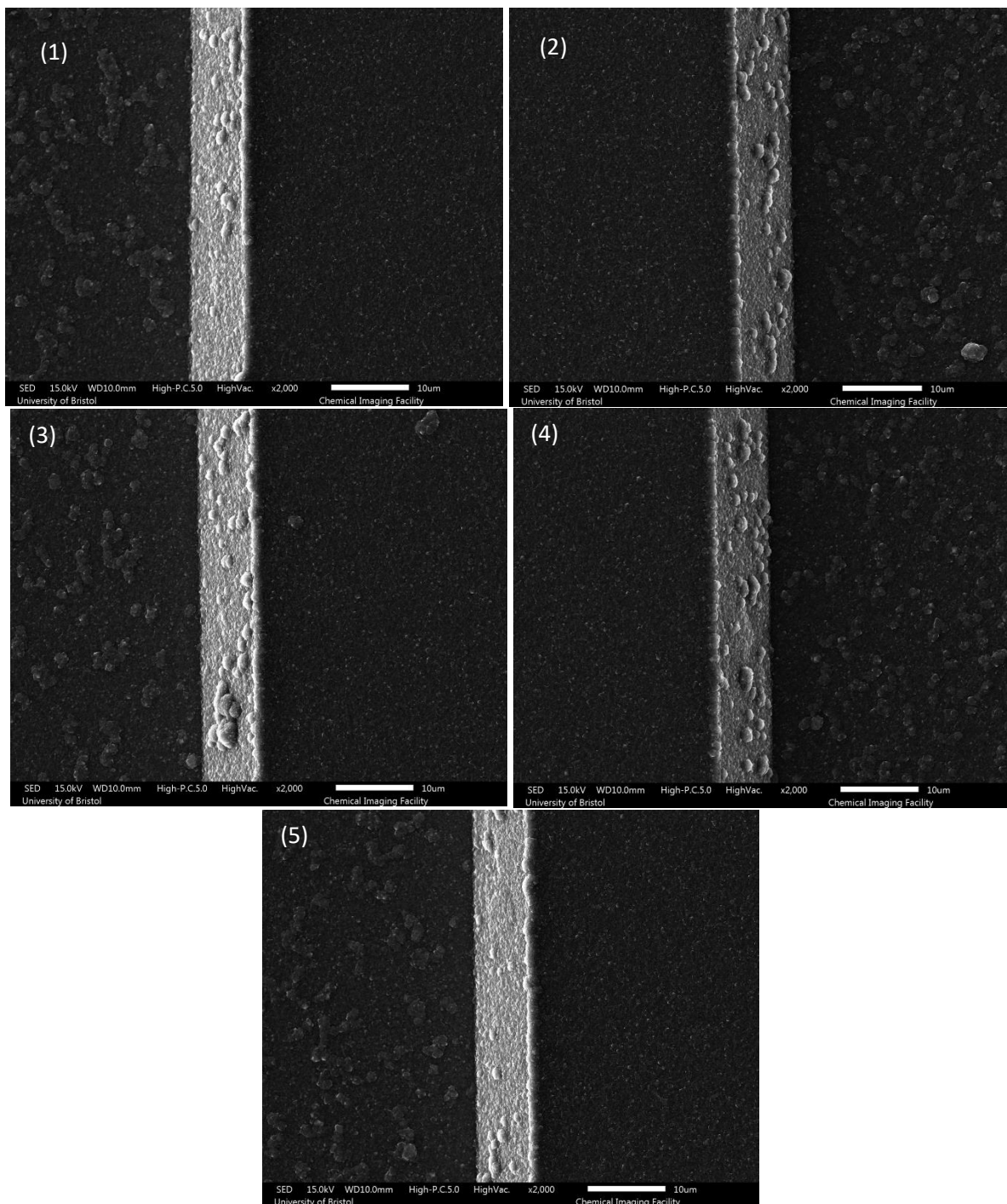


**Figure A.4:** SEM image of the left-side pattern lines of sample IS5. Diamond grown on Si plate for 6.5 h. Image 1 is the innermost line, each image moves out 1 line. Images 1-5 were taken at  $\times 2,000$  magnification. The SEM images were taken by Dr Jean-Charles Eloi of the University of Bristol's Chemical Imaging Facility.

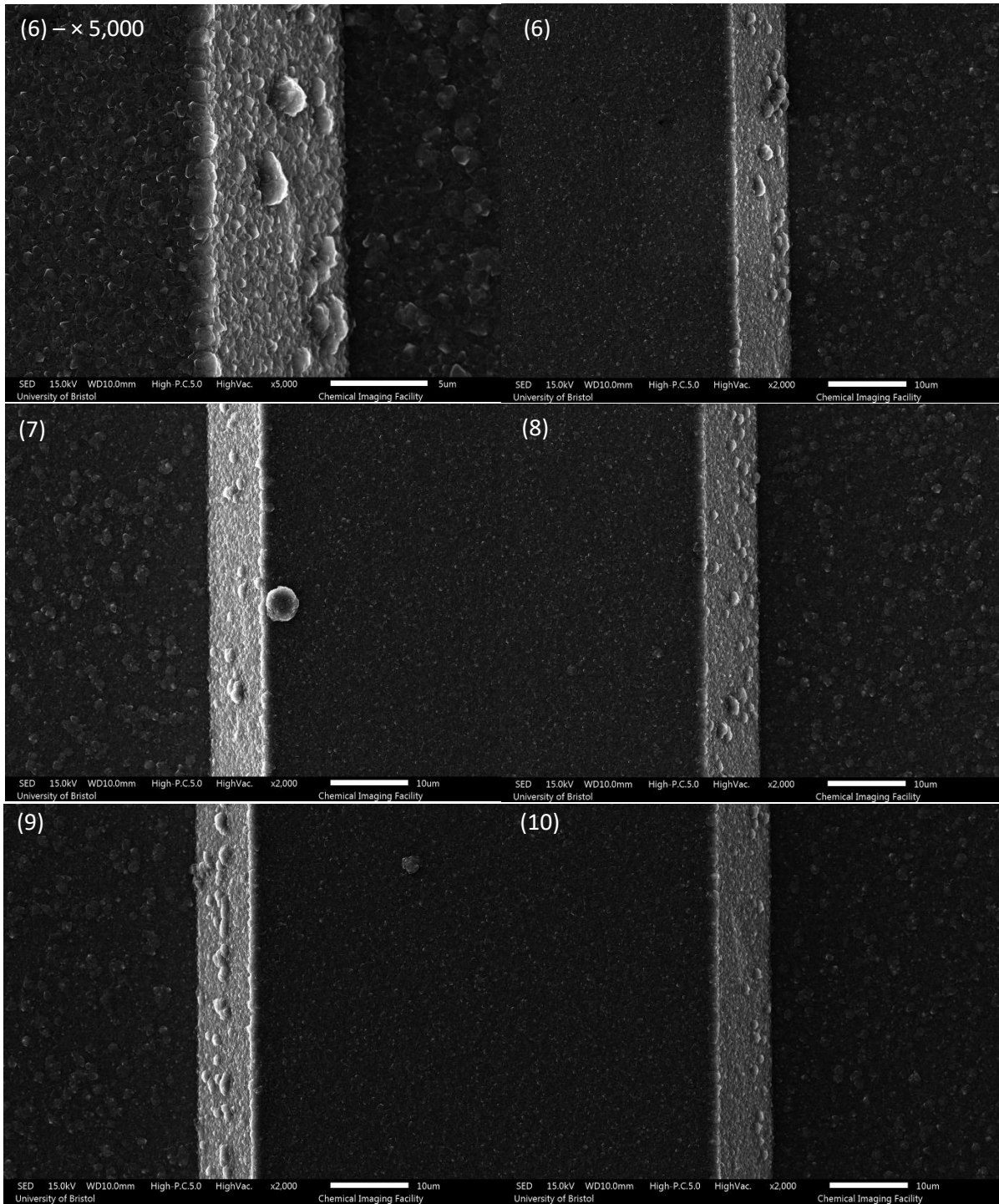


**Figure A.5:** SEM image of the left-side pattern lines of sample IS5. Diamond grown on Si plate for 6.5 h. Image 6 is the 6<sup>th</sup> line from centre, each image moves 1 line outwards. Image 6 –  $\times 5,000$  was taken from  $\times 5,000$  magnification. Images 6-10 were taken at  $\times 2,000$  magnification. The SEM images were taken by Dr Jean-Charles Eloi of the University of Bristol's Chemical Imaging Facility.

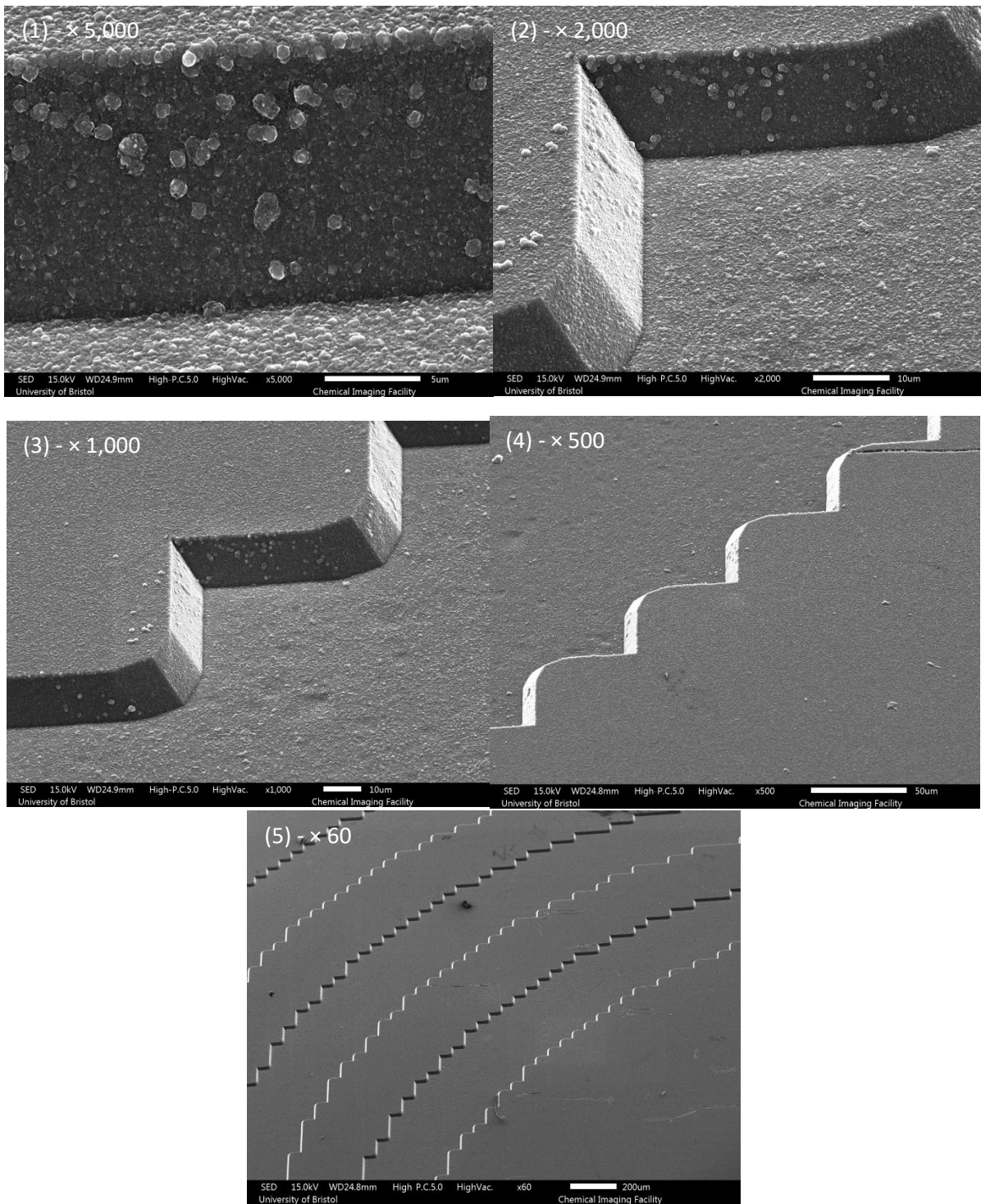


**Figure A.6:** SEM image of the left-side pattern lines of sample IS5. Diamond grown on Si plate for 6.5 h. Side wall images taken at (1)  $\times 5,000$  (2)  $\times 2,000$  (3)  $\times 1,000$  (4)  $\times 500$  and (5)  $\times 60$  magnification. The SEM images were taken by Dr Jean-Charles Eloi of the University of Bristol's Chemical Imaging facility.